THESIS FOR THE DEGREE OF LICENTIATE OF ENGINEERING

Focal Plane Arrays for Millimeter-Wave Beam-Steering Wireless Backhaul Antenna Systems

Viktor Chernikov

Department of Electrical Engineering
Chalmers University of Technology
Gothenburg, Sweden, 2025

Focal Plane Arrays for Millimeter-Wave Beam-Steering Wireless Backhaul Antenna Systems

Viktor Chernikov

Department of Electrical Engineering
Chalmers University of Technology
SE-412 96 Gothenburg, Sweden
Phone: +46 (0)31 772 1000

Printed by Chalmers Reproservice
Gothenburg, Sweden, September 2025

Abstract

The rapid expansion of communication infrastructure and development of 5G/6G communication networks aim to reach the multi-gigabit-per-second (multi-Gbps) data rates by utilizing the millimeter-wave (mmWave) frequency bands, particularly, E-, W-, and D-bands. Hovewer, well-established solutions presented on the market face scalability challenges at the higher frequencies due to low energy efficiency, limited transmitter output power, and increased path loss. Hence, this goal is impossible to achieve without hardware advancements in electronics, antenna systems, and their co-integration.

One of the key applications for 5G/6G systems is wireless backhaul, which offers flexible and cost-effective network deployment by connecting base stations to core networks using point-to-point communication links. In this context, to overcome the aforementioned challenges, antenna systems must achieve high Effective Isotropic Radiated Power ($EIRP$), which requires high-gain ($>$ 50 dBi) antenna systems operating at E-/W-band frequencies with transmitters incorporating power-combining from multiple active devices to increase output power, the signal-to-noise ratio (SNR) on the receiving side, and, thereby, achievable data rate.

The high-gain antennas have narrow beams, *e.g.* 0.5° half-power beamwidth (HPBW), which causes the problems of misalignment due to mast swaying leading to signal fading. To resolve this issue, the antenna system needs to incorporate beam-steering functionalities.

This Licentiate thesis explores solutions to address the aforementioned challenges using electronic beam-steering antennas. First, we present a comparative analysis of the existing beamforming strategies for antenna system implementation and integration with the transmitter front-end. Based on the findings of this analysis, a reflector antenna system fed by a waveguide-based (WG) focal plane array (FPA) is proposed. The baseline design considerations explore the reflector and FPA designs, identifying suitable reflector optics and FPA architecture. As a result, two focal plane array designs are proposed and implemented using inter-element decoupling, and beam-shaping techniques for performance enhancement. The proposed FPAs demonstrate $52-68\%$ aperture efficiency, < -25 dB mutual coupling levels, and 1° (2HPBW) 2D beam-steering range with the gain loss < 6 dB.

The proposed designs will be used in the active reflector antenna system demonstrator, including integration with the active transmitter front-end.

Keywords: focal plane array (FPA), high-gain reflector antenna, mast swaying, beam-steering.

List of Publications

This thesis is based on the following publications:

[A] **Viktor Chernikov**, Artem Vilenskiy, Marianna Ivashina, "Analysis of Millimeter-Wave Array Frontend Architectures for High EIRP: Comparing Various Beamforming and Power Combining Techniques". 19th European Conference on Antennas and Propagation, EuCAP 2025, Stockholm, Sweden, 2025-03-30 - 2025-04-04.

[B] **Viktor Chernikov**, Artem Vilenskiy, Marianna Ivashina, "Design Considerations for Focal-Plane Array Antennas for 6G Millimeter-Wave Backhaul Links". 2023 IEEE International Symposium on Antennas and Propagation and USNC-URSI Radio Science Meeting, AP-S/URSI 2023 Portland, USA, July 2023..

[C] **Viktor Chernikov**, Artem Vilenskiy, Sam Agneessens, Lars Manholm, Malcolm Ng Mou Kehn, Marianna Ivashina, "A Teflon-Filled Open-Ended Circular Waveguide Focal-Plane-Array Used for Sway Compensation in W-band 50dB-Gain Backhaul Reflector Antennas". 25th International Conference on Electromagnetics in Advanced Applications, ICEAA 2023, Venice, Italy, 2023-10-09 – 2023-10-13.

[D] **Viktor Chernikov**, Artem Vilenskiy, Sam Agneessens, Lars Manholm, Marianna Ivashina, "A W-Band Choke-Ring Encircled Focal Plane Array of Full-Metal Elements for Reflector Antennas with over 50%-Efficiency High Cross-Over Beams". IEEE Antennas and Wireless Propagation Letters, Vol. 23, Issue 12, pp. 4578-4582, Dec. 2024.

Other publications by the author, not included in this thesis, are:

[E] Sohaib Yaqoob Chaudhry, **Viktor Chernikov**, Artem Vilenskiy, Sam Agneessens, Lars Manholm, Marianna Ivashina, "A Compact W-band Diplexer for Integration with an Electronically Steerable Focal Plane Array Antenna System". *31st Asia-Pacific Microwave Conference, APMC 2023*, Taipei, Taiwan, Dec. 2023.

[F] Iaroslav Shilinkov, **Viktor Chernikov**, Rob Maaskant, Marianna Ivashina, "Antenna Characterization by the Back-Scattering Measurement Method Using the Integrated RF-Frontend as Load Modulation Device". *2024 International Conference on Electromagnetics in Advanced Applications (ICEAA)*, Lisbon, Portugal, Sept. 2024.

[G] Artem Vilenskiy, Yingqi Zhang, Vessen Vassilev, **Viktor Chernikov**, Marianna Ivashina, "Wideband Reflection-Type p-i-n Diode Phase Shifters in GaAs MMIC Technology at W-Band". *18th European Microwave Integrated Circuits Conference, EuMIC 2023*, Berlin, Germany, Sept. 2023.

Acknowledgments

I would like to express my sincere gratitude to my supervisor, Prof. Marianna Ivashina, for her invaluable guidance, continuous support, and encouragement throughout this research. Her insights and contributions have played a crucial role in shaping both the direction and the outcomes of this work.

My deepest gratitude goes to my co-supervisors, Dr. Artem Vilenskiy and Dr. Pavlo Krasov, for their significant contribution to the development of this research, and support me on this journey, no matter the challenges. I am also grateful to Dr. Oleg Iupikov for his valuable discussions and continuous support throughout my studies. Special thanks to Prof. Rob Maaskant, Prof. Ashraf Uz Zaman, and Prof. Jian Yang for generously sharing their expertise and knowledge during this time.

I am thankful to my examiner, Prof. Paolo Monti, for his thoughtful and kind encouragement.

This research would not have been possible without the contributions of Sam Agneessens and Lars Manholm from Ericsson Research, Marcus Gavel and Göran Granström from Gotmic AB, and my colleagues and friends at the Department of Microtechnology and Nanoscience. Thank you for sharing your expertise and broadening my perspective.

I would also like to thank all members of the Antenna Group for invaluable time spent together and for stimulating discussions.

Finally, I would like to acknowledge the funding support from VINNOVA for the "ENERGETIC" project (2021-01337) and from the Swedish Foundation for Strategic Research (SSF) for the Sweden–Taiwan Collaborative Project "Antennas Beyond 5G", which provided the financial foundation for this research.

Acronyms

5G/6G:	Fifth/Sixth Generation (Mobile Networks)
Gbps:	Gigabits per second
mmWave:	Millimeter-Wave

EIRP:	Effective Isotropic Radiated Power
HPBW:	Half-Power Beamwidth
FPA:	Focal Plane Array
WG:	Waveguide
SNR:	Signal-to-Noise Ratio
Tx:	Transmitter
Rx:	Receiver
PA:	Power Amplifier
PAE:	Power-Added Efficiency
FWA:	Fixed Wireless Access
IoT:	Internet of Things
ETSI:	European Telecommunications Standards Institute
RFIC:	Radio Frequency Integrated Circuit
RF:	Radio Frequency
PCB:	Printed Circuit Board
EEP:	Embedded-Element Pattern
EM:	Electromagnetic (field)
PC-BF:	Power-Combining Beamforming (Network)

Contents

Part I

Overview

CHAPTER 1

Introduction

1.1 Motivation

The extensive growth of high-data-rate applications is pushing the boundaries of existing wireless communication systems. In this context, the intensively developing 5G/6G communication networks offer data rates 10 times faster than the previous generation, far above 10 Gbit/s, and includes use cases, such as fixed wireless access (FWA), the Internet of Things (IoT), and wireless backhaul [1]. The latter is dedicated to interconnecting base stations with core networks, thereby, being the key technology that supports scalable network architectures by enabling more flexible and cost-effective infrastructure deployment [2]. This becomes especially important in remote areas where wireline backhaul deployment utilizing optical fiber is economically impractical. In this context, an antenna system becomes a crucial component in ensuring the high performance and reliability of wireless backhaul links.

The maximum Shannon's channel capacity of the communication link ($C_{\max}$) with specified bandwidth (B) in the presence of Gaussian noise is determined

by the Shannon–Hartley theorem:

$$C = B \log_2(1 + SNR), \tag{1.1}$$

where SNR is the signal-to-noise ratio. This expression defines the main directions of the development of communication links, specifically the increase in absolute bandwidth and SNR. This drives the expansion of the utilized spectrum to the mmWave frequency ranges, particularly E-/W-bands, which offer abundant spectrum for multi-Gbps wireless links, demonstrating high performance in point-to-point communication backhaul [3]. However, operation in the mmWave frequency range faces severe challenges related to the signal propagation. For point-to-point communication link in line-of-sight, they can be specified using Friis equation:

$$P_{\mathrm{Rx}} = P_{\mathrm{Tx}} G_{\mathrm{Tx}} G_{\mathrm{Rx}} \left(\frac{\lambda}{4\pi R} \right)^2 \tag{1.2}$$

where P_{Rx} is the received power, P_{Tx} is the transmitted power, G_{Tx} is the transmitting antenna gain, G_{Rx} is the receiving antenna gain, λ is the wavelength in the free space, and R is the distance between the receiving and transmitting antennas (Fig.1.1). From 1.2, the following challenges can be outlined:

1. **Limited power generation of electronic components:** P_{Tx} is determined by the Johnson limit (Fig. 1.2), and depends on the semiconductor process utilized in transmitter (Tx) front-end design. Thus, according to [4], the power amplifiers (PAs) designed in the technological processes available today demonstrate the degradation of the saturated power (P_{sat}) at a higher operational frequency. In particular, the PAs implemented in the most mature processes, such as CMOS and SiGe BiCMOS, rarely demonstrate the $P_{\mathrm{sat}} > 20$ dBm with power-added efficiency (PAE) around 17% at W-band frequency ranges [5], [6]. The devices implemented in III-V processes, such as GaN and GaAs, facilitate the highest P_{sat} ($27 - 30$ dBm) with relatively high PAE (10% for GaAs and 15% for GaN) [7], [8].

2. **High free-space path loss:** the term $\left(\frac{\lambda}{4\pi R}\right)^2$ corresponds to the scattering of the EM field in the free space. This mechanism leads to a significant reduction in the receiving power at the mmWave frequencies,

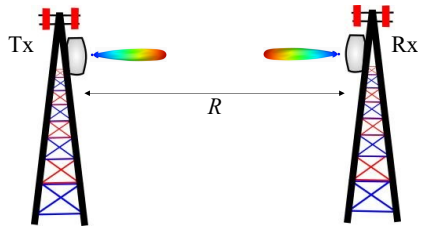

Figure 1.1: The illustration of line-of-sight communication link (point-to-point).

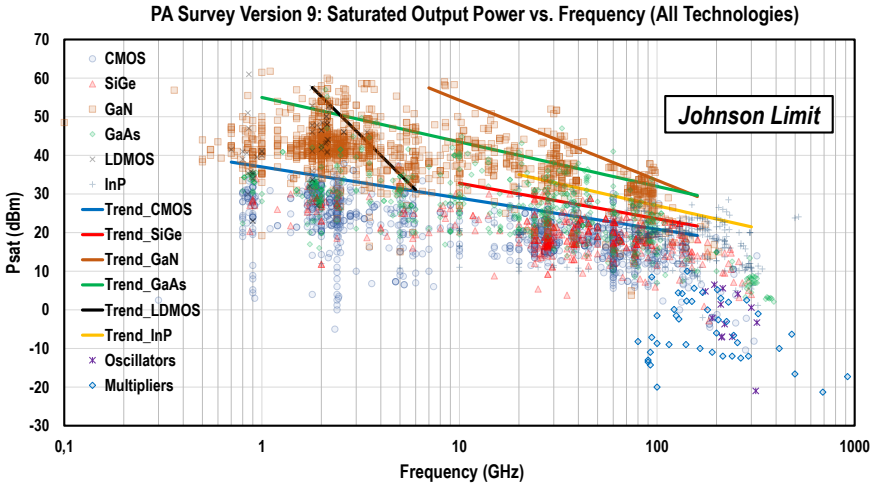

Figure 1.2: Saturated power vs. frequency (All Technologies) from the cited PA works since 2000 [4].

e.g. the ratio between the received power levels at 9 GHz and 90 GHz is 20 dB at the same distance.

3. **Atmospheric attenuation:** the additional attenuation of the electromagnetic (EM) field, due to the molecular properties of the gases contained in the air and poor weather conditions (Fig. 1.3).

One of the ways to address these challenges is the increase in the density of point-to-point backhaul links, which significantly increases the cost of the

network deployment and scaling. Another way is to utilize a transmitter (Tx) architecture that allows the use of ultra-high-gain antennas (> 50 dBi) in combination with efficient power-combining techniques in transmitter design. This approach can overcome the above-mentioned challenges and facilitate a stable communication link, with a multi-Gbps data rate network [9]. In this context, maximization of the effective isotropic radiated power ($EIRP$), defined as $EIRP = G_{\mathrm{Tx}} P_{\mathrm{Tx}}$, becomes crucial in the design of such systems.

As a result, mmWaves is a key enabler for high data rate 5G/6G communication networks. However, severe challenges must be addressed in communication system development to fully realize the offered potential.

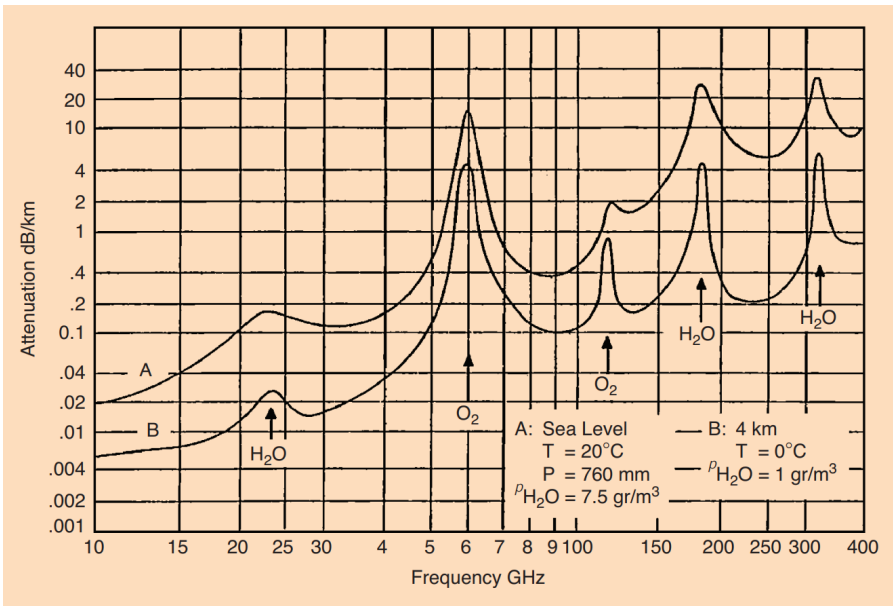

Figure 1.3: Average atmospheric absorption of millimeter waves [10].

1.2 Design Challenges for High-EIRP mmWave front-ends

The problem of the $EIRP$ maximization in the mmWave frequency range is accompanied by a variety of design and implementation challenges, such as:

1. **Feasibility of the solution:** a solution for the antenna system and Tx front-end must have reasonable complexity and be compatible with the standard interfaces.

2. **The ETSI class 3 side-lobe mask compliance [11]:** the requirements for the side-lobe level add complexity to the antenna design.

3. **The choice of the technological process for electronic components (RFICs):** RFIC implementation is a trade-off between performance and commercial availability.

4. **High antenna aperture efficiency:** ultra-high gain antennas require efficient use of the aperture due to constraints on weight and volume.

5. **High radiation efficiency of the antenna system with an electrically large aperture:** The insertion loss of the feeding network and the antenna system itself after the final amplification stage significantly impact the efficiency of the entire transmitter.

6. **Efficient power-combining and/or beamforming techniques:** antenna system and Tx front-end architecture define the feeding, power-combining, and beamforming strategies and their implementation that affect the efficiency of the entire transmitter.

7. **Misalignment between the receiving and transmitting antennas in the communication link:** ultra-high gain antennas are capable of generation of > 50 dBi beams that typically have $\approx 0.5°$ half-power beamwidth (HPBW). This leads to a high sensitivity to misalignment, resulting in a significant gain reduction in practical deployment scenarios.

Regarding the last challenge, Ericsson has reported the effects related to signal fading (SNR reduction) in wireless backhaul links due to antenna mast

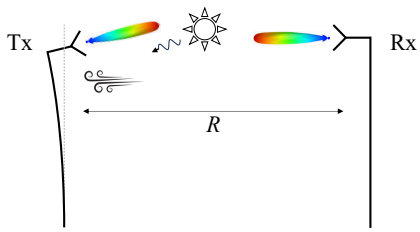

Figure 1.4: Illustration of mast swaying in the line-of-sight communication link.

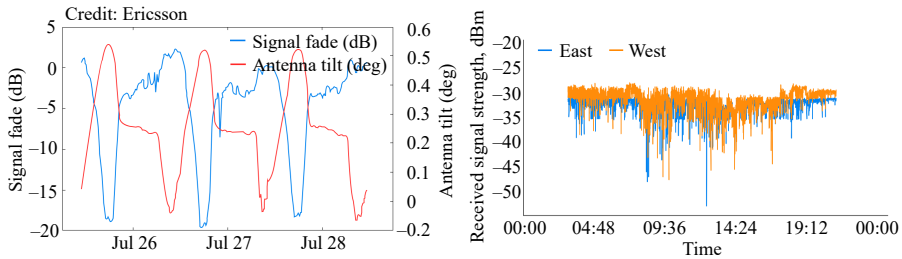

Figure 1.5: The impact of the antenna must sway on the receiving signal fading due to (a) sunflower effect [12] and (b) windy weather conditions [13]. (the illustration was modified to improve compatibility with the format of the thesis)

sway caused by various weather conditions [12], [13]. The tracking of the receiving power was carried out using the E-band backhaul link with 50 dBi reflector antennas. Fig. 1.5 demonstrates the impact of the antenna mast sway on the signal fade, in particular, > 20 dB signal fade can be observed due to the antenna tilt at 0.5°. As a result of these studies, two mast sway scenarios can be outlined:

1. Slow sway with a rate of 0.5° per day, which is caused by thermal expansion due to sunlight illumination (sunflower effect) [12], causing antenna mast deformation [Fig. 1.5(a)].

2. Fast sway with a rate of 0.5° per second due to wind and support vibration [Fig. 1.5(b)].

To address the above-mentioned challenge, the development of an antenna system capable of rapid beam-steering in the 1° 2D angular range needs to be considered. This conclusion emphasizes the importance of addressing the fifth challenge: the choice of the power-combining and beamforming approaches and their implementation is the factor determining the backhaul link performance.

In summary, antenna mast swaying and limited power generation capabilities are especially critical at E-/W-bands, and result in significant SNR degradation. Therefore, the high $EIRP$ antenna system with integrated Tx front-end capable of the efficient power-combining and beam-steering can be considered as a key to the successful development of 5G/6G communication networks.

1.3 High-EIRP Beam-Steering Antenna Systems Overview

Literature survey illustrates a sparse set of solutions for antenna systems capable of beam-steering (and potentially tracking) at E-/W-band frequency ranges. However, the available examples including ones operating at mmWave frequencies around K_a-band can be considered as the starting point for design suitable for E-/W-band backhaul application.

Phased Array Antenna Systems

Phased array antenna represents the most common solution for applications requiring beam-steering functionality. However, while offering high beamforming flexibility, in the case of the ultra-high gain antenna, its implementation requires a significant number of RFICs, resulting in an extremely high cost. Another drawback is the difficulties in the implementation of phased arrays at E-/W-band frequencies due to manufacturing tolerances and increased material loss. Waveguide (WG) based architectures facilitate high radiation efficiency and robustness, but are challenging to integrate RFIC [19]–[21]. Therefore, most phased arrays are realized as antenna-on-chip or antenna-in-package (AiP) in this frequency range [14], [22]–[25]. Taking into account the small scanning range and high gain ($>$ 50 dBi) required for the targeted application, AiP phased arrays would need an excessive number of elements.

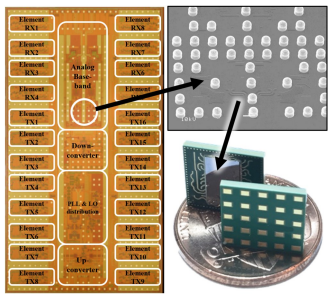

(a) W-band patch antenna phased array integrated with SiGe BiCMOS RFIC [14]

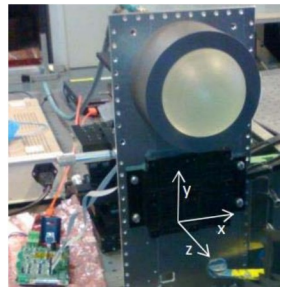

(b) E-band dielectric lens with feed array [15]

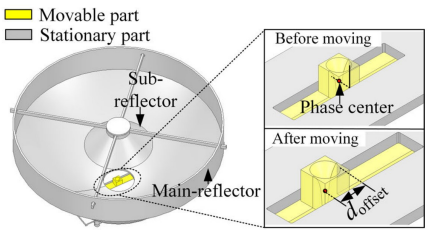

(c) W-band Gregorian dual-reflector with movable feed [16]

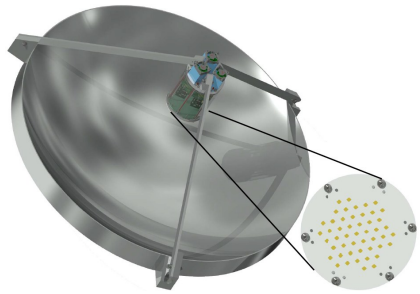

(d) K_a-band spherical reflector with active FPA [17]

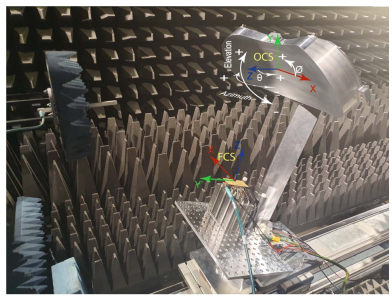

(e) K_a-band torus reflector with active FPA [18]

Figure 1.6: The state-of-the-art beam-steering antenna systems.

In terms of the Tx output power, the phased array, depicted in Fig. 1.6a achieve $\approx$ 52 dBm of the peak $EIRP$ utilizing the RFICs in 0.18-μm SiGe BiCMOS [14]. Notably, this is equivalent to a Tx output power of 2 dBm only if using an efficient ultra-high gain antenna, while the targeted application calls for, at least, 25 dBm.

Quasi-optical Antenna Systems

As an alternative, quasi-optical antenna systems can be used for beam-steering within narrow angular ranges [26], [27]. Among them, the dielectric lens antenna is a popular solution for high-gain applications [Fig. 1.6b]. However, dielectric antennas along with different types of printed antennas have a radiation efficiency around $25 - 30\%$, making them unsuitable for wireless backhaul links [15], [28], [29]. At the same time, parabolic reflector antennas have already recommended itself in E-band fixed beam backhaul links [13]. Moreover, the implementation of beam-steering capabilities has been successfully demonstrated in the previous works [16]–[18], [30], [31]. Here, the proposed solutions include mechanical and electronic beam-steering approaches.

Mechanical beam-steering

For instance, the work [16] introduces Gregorian dual-reflector system with movable feed based on gap WG technology (Fig. 1.6c), offering $\pm 2^\circ$ 1D angular range. In addition, the possibility of 2D beam-steering was also demonstrated in [32]. The high radiation efficiency, antenna gain above 50 dBi, and proposed mechanical beam-tracking system represents unique advantages of this solution. However, the mechanical scanning approach cannot address the fast mast swaying due to the high inertia of the beam-tracking system. Furthermore, the dual-reflector systems have large volume and demand high positioning accuracy of the feed, sub-reflector, and main reflector, which makes such implementation difficult and costly at mmWave frequencies. In this way, positioning errors and blockage from sub-reflector results in aperture efficiency of $37 - 46\%$, which is rather low for such reflector systems. Moreover, the side-lobe mask compliance is challenging for this design.

Electronic beam-steering

Alternative examples using electronic beam-steering with an antenna array in the focal plane are presented in [17], [18], [30], [31]. Among them, the work [17] addresses the challenges related to the side-lobe level requirements, 2D scanning range of 8°, and the $EIRP$ level of 66 dBm using a spherical prime-focus reflector fed by a PCB-based focal plane array (FPA), comprising 7 clusters of 7 patch antennas in each with integrated Tx front-end (Attenuator+PA per element) [Fig. 1.6d]. Here, the reflector choice is motivated by the near-zero beam-scan loss with the penalty of aperture efficiency around 28% and antenna gain of 36 dBi for the aperture diameter of 0.6 m. The work [18] shows a solution with a torus reflector fed by PCB-based FPA comprising 324 active elements with integrated SiGe BiCMOS PAs (Fig. 1.6e). This yields the $EIRP$ of 60 dBm and antenna gain of 36 dBi in the 1D scanning range of ±30°, and the reflector shape also facilitates near-zero beam-scan loss (aplanatic optics). These results demonstrate the potential to achieve high $EIRP$ and increase the distance of communication link. However, the electronic integration aspects still remain a challenge at E-/W-band frequencies. A comparative analysis of existing solutions exploiting mechanical and electronic beam-steering is summarized in Table. 1.1.

The main advantages of the electronic beam-steering approach compared to the mechanical one are the speed of beam-steering and beamforming flexibility, which allows introducing beam-tracking functionality without additional system modification. Following this approach, in this work, a single offset parabolic reflector fed by FPA is chosen as the baseline design for further research. This decision is mainly motivated by the necessity of high antenna aperture efficiency in order to reduce maximal system dimensions while facilitating the required $EIRP$. It is worth mentioning that reflector antennas with $F/D < 0.5$ are preferable in this case to maintain a relatively small FPA and mitigate the far-out side-lobe level for the far-field pattern mask compliance [33].

Table 1.1: High-EIRP antenna solutions suitable for mmWave frequencies

System configuration	# of active channels	# of array elements	Frequency, GHz	Scanning approach	Scanning range	Peak $EIRP$, dBm
Patch antenna phased array integrated with RFIC [14]	256	256(Tx) / 128(Rx)	$95-109.5$	Electronic	30°, 2D	52
Gregorian dual-reflector with movable feed [16]	N/A	1	$71-86$	Mechanical	±2.5°	N/A
Spherical reflector with active FPA [17]	49	49	$28-32$	Electronic	8°, 2D	66
Torus reflector with active FPA [18]	324	324	$26-30$	Electronic	±30°, 1D	60
Dielectric lens with feed array [15]	1	64	$71-76$ / $81-86$	Electronic	±4° × ±17°, 2D	34

1.4 Focal Plane Array Overview

Initially, FPAs found their application in radioastronomy as a part of multi-beam radio telescopes with an extended field of view (FoV) [31], [34]. The proposed concept used dense FPAs (with inter-element spacing $< 0.5\lambda$) with a large number of elements (≈ 100 elements and ≈ 36 beams), which provide continuous and wide FoV, but make it very expensive [35]. The attempts in adaptation of FPA-fed reflector antenna systems for communication purposes resulted in trade-offs between the quality of FoV and cost optimization. In particular, the preferable reduction of element number in the array can result in either narrowing of the FoV (or scanning range for the Tx case), or beam cross-over level and aperture efficiency degradation, when increasing inter-element spacing [18], [34].

Published FPA designs operating in the K_a-band employ mainly patch elements [Figs. 1.7a, 1.7b] [17], [18]. Due to this PCB-based FPA implementation, these solutions are not scalable to the E- or W-band because of the intrinsically low radiation efficiency. Despite this, there are some examples of printed [36] and on-chip [37] FPA solutions in the W-band, that, consequently, have a low $EIRP$. Alternatively, FPA designs utilizing metal elements, such as horns [38], [39], gap WGs [16], [40], and patch-excited cups [41], shown in Fig. 1.7, demonstrate higher radiation efficiency, however, their large apertures ($\gg \lambda$) cause the cross-over level < -10 dB for reflector antennas with $F/D < 0.5$ [34], if a complex multi-reflector system is not employed. This challenge can be resolved by miniaturization of the FPA element, *e.g.* partial/complete filling of the WG with dielectric material [42], [43]. This approach adds manufacturing and assembly complexity and trades radiation efficiency of the FPA for scanning performance improvement, in particular, caused by reduction of the inter-element spacing down to 0.75λ. This yields the improved cross-over level of > -6 dB for parabolic reflectors with $F/D = 0.3 - 0.5$.

The aforementioned solutions and their drawbacks demonstrate the necessity to explore FPA designs addressing the challenges, such as high radiation efficiency, small proximity between the elements (high beam cross-over level), and manufacturing and assembly feasibility.

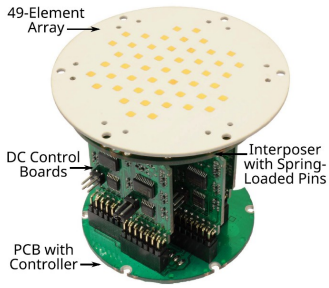

(a) PCB-based patch FPA feed for the spherical reflector [17]

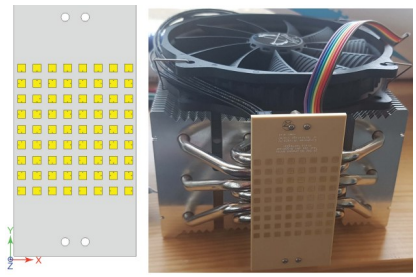

(b) PCB-based patch FPA feed for teh torus reflector [18]

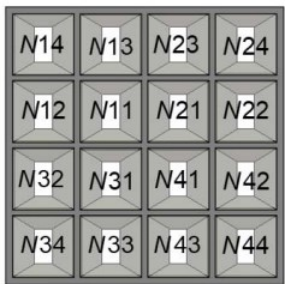

(c) W-band pyramidal horn FPA feed for Cassegrain reflector antenna [38]

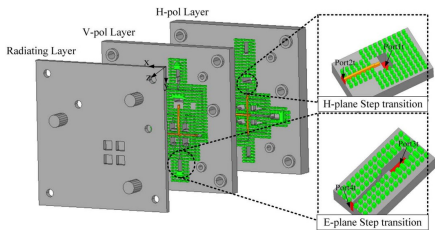

(d) Monopulse feed for Cassegrain reflector antenna [40]

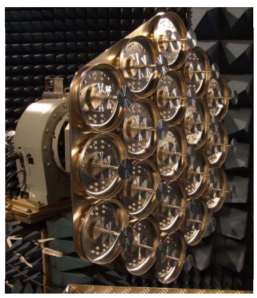

(e) Patch-excited cup FPA [41]

Figure 1.7: The state-of-the-art FPA feed design examples.

1.5 Power-Combining and Beamforming Techniques for Active Antenna Systems

As mentioned above, mmWave communication networks need active beam-steering antenna systems. Thus, in addition to antenna system design, Tx front-ends of such systems should jointly provide power-combining and beamforming functionalities. The work [44] outlines the strategies commonly utilized in active antenna arrays. Based on these findings, the analysis can be extended to the level of components and their contribution to system-level performance such as Tx output power, and $EIRP$.

Power-Combining

Here, power-combining approaches are considered on the circuit level (power-combiner is integrated into the circuit) and the external component level. The Table. 1.2 summarizes the performance of some existing power-combiners along with their implementation technologies.

Table 1.2: The examples of the existing power-combining approaches.

Power-combiner type	**Implementation**	**Typical insertion loss, dB**
Corporate	Microstrip, On-chip (Wilkinson [45], [46])	$2\log_2(N)$ (W-band)
	WG [47]	0.4 (W-band)
Radial	Coaxial line [48]	1 (C-band)
	Silicon micromachining [49]	1 (W-band)
	WG [50]	0.8 at 200 GHz
Spatial	Microstrip [51]	2 (X-band)
	Substrate Integrated Waveguide (SIW) [52]	1 (K_a-band)
	WG [53]–[55]	2 (W-band)

In this context, it is reasonable to consider the on-chip and WG power

combiners only as those commonly used in the E- and W-bands. Notably, this choice provides the limits of the achievable power-combiner performance in terms of insertion loss, which is one of the main factors that affects Tx output power.

Beamforming

Regarding beamforming approaches, the conventional phased array, Butler matrix [56], [57], or Rotman lens [58] can be utilized for reconfiguration of the far-field pattern. Among them, the latter two require a switching network to be connected to their inputs to generate different far-field patterns. In the E- and W-bands, the insertion loss of the switching matrix can be evaluated as $2.5 - 3$ dB per single-pole-2-through switch or $6 - 8$ dB per single-pole-4-through switch which significantly impacts system-level performance [15].

The work [44] proposes the concept of unified power-combining and beamforming (PC-BF) network, which allows to combine the power from multiple active devices into the output ports. The operational principle is based on the simultaneous excitation of the array of device inputs with certain amplitudes and phases, and their "radiation" into the quasi-optical region. The EM field distribution at the array of the output ports is defined by the excitation of the input ports, facilitated by phase shifters and PAs. Therefore, when connected to antenna array elements, this network can act as a beamformer when the combined power of multiple PAs is delivered to the antenna, except for the insertion loss.

Thus, the analysis can be limited by considering two principal conventional architectures, *i.e.* the reflector antenna with phased array feed and element-level power-combining (architecture #1) [Fig. 1.8a], modular design with separate power-combining and beam-switching networks (architecture #2) [Fig. 1.8b] and the proposed one modular design with unified PC-BF network (architecture #3) [Fig. 1.8c]. The design of the FPA utilized in this analysis is presented in Chapter 3.

Scalability analysis is performed for the considered architectures, based on the available data in the literature. Here, the PA output power $P_{\mathrm{PA}}^{\mathrm{out}} = P_{\mathrm{sat}} =$ 24 dBm [59], the maximum achievable Tx output power is $P_{\mathrm{max}}^{\mathrm{out}} = N \times P_{\mathrm{PA}}^{\mathrm{out}}$, D_{max} is the maximum achievable directivity of the reflector aperture, and $EIRP_{\mathrm{max}}$ is the maximum achievable $EIRP$. The Tx output power and $EIRP$ are computed for all architectures beamformed in the broadside and

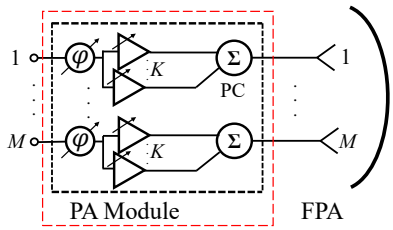

(a) Architecture #1

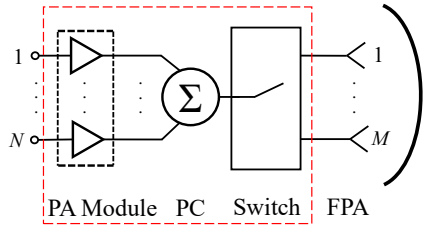

(b) Architecture #2

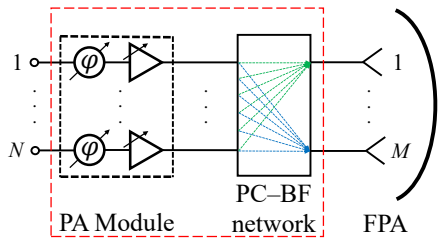

(c) Architecture #3

Figure 1.8: The FPA-fed reflector antenna system with Tx front-end architectures considered as suitable for the W-band operation. Here, K is the number of PAs per element in architecture #1, N is the number of active channels in architectures #2 and #3, and M is the number of FPA elements.

are shown in Fig. 1.9. The obtained results demonstrate the benefits of using the unified PC-BF network as a feeding network for the FPA, which allow to facilitate the achievable $EIRP_{\max}$ by $5-10$ dB higher.

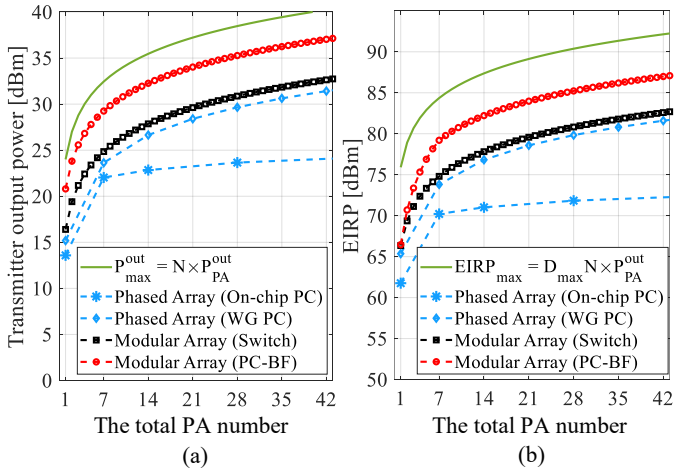

Figure 1.9: Scalability analysis for the Tx architectures: (a) $EIRP$ and (b) Tx output power vs. number of PAs for the on-axis beam.

1.6 Problem Formulation and Scientific Contribution

In the context of the provided motivation, the main research problem for the PhD project can be defined as the development and experimental demonstration of the active antenna system capable of beam-steering within the 1° 2D angular range with high Tx output power and $EIRP$ for antenna mast swaying compensation. The generalized block diagram of the system is shown in Fig. 1.8c.

In particular, this licentiate thesis is focused on the development of FPAs that are suitable for W-band ($92-96$ GHz) operation and addresses the main design challenges in antenna design, such as high radiation efficiency, efficient illumination of the reflector, and high cross-over level of the adjacent beams. As a result of this work, the following scientific contribution are established:

- The analysis of mmWave Tx front-end architectures for high-EIRP point-to-point applications comparing different power-combining and beam-forming techniques. This work covers available Tx front-end architectures and comparison of their performance in terms of the Tx output

power and $EIRP$. This motivates the choice of the reflector antenna system type suitable for high-EIRP point-to-point applications, and proposes the system architecture addressing the existing challenges (**Paper A**).

- The baseline design considerations are presented for the 7-element FPAs utilized for the prime-focus parabolic reflector antenna. The work determines the required inter-element spacing for the array, trade-offs between the efficiency and cross-over level in the choice of the reflector (F/D), and the comparison of the considered designs regarding the practical feasibility and integration at the later stage (**Paper B**).

- Design of a new teflon-filled circular open-ended waveguide FPA and its experimental validation. The work shows the development of the design flow and optimization for the small-element-number FPAs, and its performance verification. As a result of this work, the main design aspects, such as element decoupling, and beam-shaping, were addressed (**Paper C**).

- Design of a new air-filled rectangular open-ended waveguide FPA and its experimental validation. The work is focused on the motivation of focal plane configuration: number of elements, the minimal size of the aperture and inter-element spacing required. The FPA performance is verified by comparison of the simulated and measured S-parameters and far-field patterns. The obtained results are used to validate the reflector antenna system performance (**Paper D**).

The aforementioned contribution results in technical solutions for the FPAs operating in W-band. This defines the path for integration of the FPA-fed reflector antenna system with the active Tx front-end.

1.7 Thesis Outline

In **Chapter** 1, the motivation and main challenges at mmWave frequencies and the general overview of high-EIRP antenna systems are provided along with the comparative analysis of potential active antenna system architectures. As a result, the implementation strategy is chosen for the system.

In **Chapter** 2, the baseline FPA-fed reflector antenna design is considered with a focus on achievable performance. Three FPA designs are proposed and cross-compared in terms of achievable performance, implementation complexity, and compatibility with existing beamforming networks.

Chapter 3 considers the implementation of the proposed FPA designs and strategies for performance enhancement. The description of the prototypes and measurement results are presented and analyzed in terms of the reflector antenna system performance.

In **Chapter** 4, the summary of included papers is provided.

Chapter 5 concludes the presented work and outlines the future research directions.

CHAPTER 2

Design Considerations for Focal Plane Arrays Based on Open-Ended Waveguide

This chapter outlines the system design goals and technical considerations for the proposed parabolic offset reflector antenna system operating in the $92 - 96$ GHz range. The required feed displacement and reflector geometry are analyzed, including comparison with traditional waveguide horn feeds. The latter motivates the choice of the FPA architecture in terms of achievable the cross-over level, and inter-element spacing. The design considerations for FPAs with three considered element types are presented and analyzed with respect to achievable performance and implementation aspects.

2.1 Design Goals

System Design Goals

The following system design goals can be formulated:

- The directivity of the reflector antenna: $D \geq 50$ dBi
- Scanning range: 1°, 2D

- Beam scan loss: ≤ 1 dB
- Cross-over level: ≥ -6 dB
- Side-lobe level: ETSI class 3
- Frequency range: $92 - 96$ GHz

The system design goals directly influence the reflector geometry. The baseline configuration of the single offset parabolic reflector antenna with $F/D < 0.5$ is motivated from the system point of view in Section 1.3, and addresses the challenges related to the side-lobe mask. The required directivity of 50 dBi can be achieved with the projected aperture diameter of the reflector $D_\mathrm{r} = 0.4$ m or larger, which requires FPA facilitates a high aperture efficiency. At the same time, a small antenna diameter makes the system less susceptible to mast sway.

To meet the other system goals, such as the scanning range, acceptable beam scan loss, and cross-over level, the design of the FPA must be tailored accordingly. This includes defining key parameters, such as inter-element spacing and the *primary* EEP (FPA EEP) beamwidth needed to achieve the desired amplitude taper at the reflector rim. These parameters are derived based on the established baseline reflector geometry and the required feed displacement, which is discussed further.

The Baseline Reflector Geometry and Required Feed Displacement

As mentioned in section 1.3, the offset parabolic reflector antenna configuration is chosen in this work, owing to its simplicity and mitigated blockage.

First, the projected aperture diameter of the reflector is chosen as $D_\mathrm{r} = 125\lambda = 0.4$ m (λ is the free-space wavelength at the central frequency), which yields the maximum directivity of 51.9 dBi at the central frequency of 94 GHz and 51.7 dBi at the lowest one. The clearance value $C_\mathrm{r} = 1.55\lambda = 5$ mm is chosen to mitigate the feed blockage. In this context, the semi-subtended angle θ_sub and the feed tilt θ_f can be calculated as functions of the focal length

F as follows [60]:

$$\begin{aligned}\theta_{\mathrm{f}}(F) &= \arctan\left(\frac{2F(D_r+2C_r)}{4F^2-C_r(D_r+C_r)}\right),\\ \theta_{\mathrm{sub}}(F) &= \arctan\left(\frac{2FD_r}{4F^2+C_r(D_r+C_r)}\right).\end{aligned} \tag{2.1}$$

Below, the dependence on F is omitted for compactness.

For the offset reflector configuration, the modified $(F/D_r)_{\mathrm{offset}}$ can be implied:

$$(F/D_r)_{\mathrm{offset}} = \frac{\cos\theta_{\mathrm{sub}}+\cos\theta_{\mathrm{f}}}{4\sin\theta_{\mathrm{sub}}} \tag{2.2}$$

Notably, if $\theta_{\mathrm{f}}=0$, this will correspond to the prime-focus illumination, and the formula gives the correct result for $(F/D_r)_{\mathrm{prime}}$ [60].

Thus, the beam deviation factor (BDF) can be determined as:

$$BDF_{\mathrm{offset}} = BDF_{\mathrm{prime}}\frac{(F/D_r)_{\mathrm{offset}}}{(F/D_r)_{\mathrm{prime}}} = \frac{16\,(F/D)^2_{\mathrm{prime}}+0.36}{16\,(F/D)^2_{\mathrm{prime}}+1}\frac{(F/D_r)_{\mathrm{offset}}}{(F/D_r)_{\mathrm{prime}}} \tag{2.3}$$

Hence, under the assumption of large reflectors, the required feed displacement (d_{f}) can be obtained as follows [60]:

$$d_{\mathrm{f}} = F\tan\left(\frac{\theta_{\mathrm{s}}}{BDF_{\mathrm{offset}}}\right), \tag{2.4}$$

where θ_{s} is the scanning angle chosen as 0.65°.

It is of interest to compare the required feed displacement with the size of conventional WG-based reflector feed, *e.g.* corrugated conical horn (CCH) antenna. The approximate diameter of the horn that generates a Gaussian beam can be evaluated, based on the equations and figures in [61]:

$$d_{\mathrm{CCH}} = \frac{\lambda_0}{\pi}\sqrt{-0.92\frac{T}{\theta^2_{\mathrm{sub}}e_{\mathrm{CCH\ ap}}}}, \tag{2.5}$$

where T is the relative level of the CCH far-field pattern at angle θ_{sub} with respect to the maximum value (amplitude taper) and $e_{\mathrm{CCH\ ap}}$ is the aperture efficiency of the horn. The latter varies between 52.2% [62] for the optimal conical horn and $\simeq 80\%$ for the corrugated horns [63].

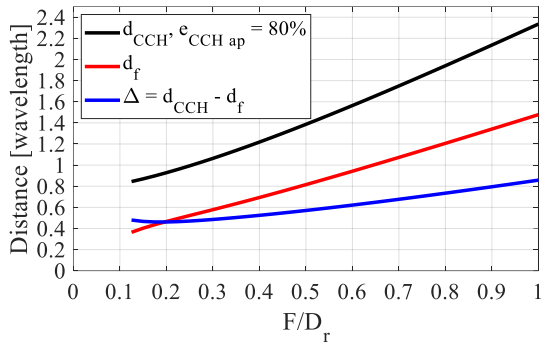

Figure 2.1: The required feed displacement for the scan at angle of θ_s and CCH diameter with $e_{\text{CCH ap}} = 80\%$ vs. reflector $(F/D_r)_{\text{prime}}$.

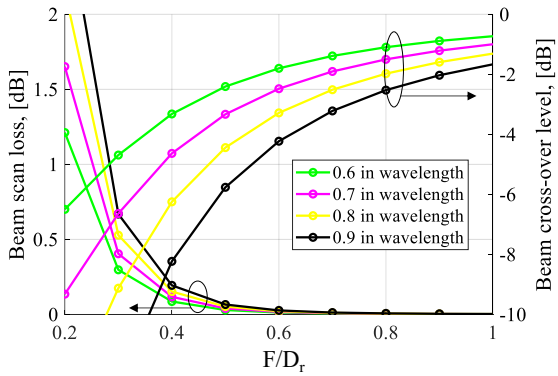

Figure 2.2: Beam scan loss and beam cross-over level vs. $(F/D_r)_{\text{prime}}$ for prime focus reflector antenna.

Fig. 2.1 illustrates the dependence of the required feed displacement d_{f} and the CCH diameter d_{CCH} on $(F/D_{\text{r}})_{\text{prime}}$ while keeping D_{r} constant. The result shows that it is potentially impossible to scan at the required θ_{s} using the CCH feed cluster because CCH diameter exceeds the required feed displacement leading to low cross-over level. At the same time, the use of another element type results in significant efficiency degradation and increase in side-lobe level.

As a potential solution, cluster of open-ended waveguides can be considered

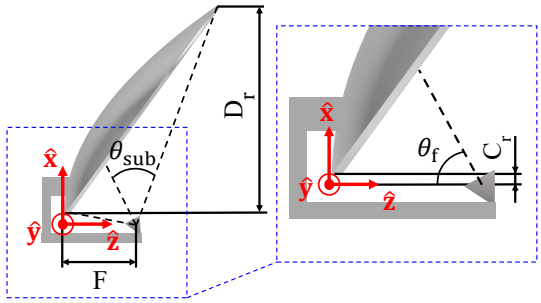

Figure 2.3: The final reflector geometry.

since it allows to synthesize an FPA with the reduced inter-element spacing. However, FPA embedded element patterns need to be shaped to facilitate high aperture efficiency. The latter sets a limitation on the minimal required FPA aperture area.

While focusing on the $(F/D_\mathrm{r})_\mathrm{prime} < 0.5$ region, the reflector antenna scanning performance can be evaluated for the inter-element spacing range of $0.6\lambda - 0.9\lambda$ using Gaussian beam model with -10 dB amplitude taper at the rim. In this particular case, it was done for the prime-focus reflector. The result is depicted in Fig. 2.2.

Based on the results presented above, the $(F/D_\mathrm{r})_\mathrm{prime} = 0.35$ in combination with the 0.75λ inter-element spacing is chosen as a trade-off between scanning performance and FPA implementation feasibility. The final reflector design is shown in Fig. 2.3.

FPA Design Goals

Based on the aforementioned considerations, the requirements for the FPA design can be formulated as follows:

- The FPA embedded pattern beamwidth at the -10 dB level $\Delta\theta_{-10\mathrm{dB}} = 120°$.
- The FPA inter-element spacing is 0.75λ.
- The aperture efficiency of the reflector antenna is $e_\mathrm{ap} > 50\%$ for all scanned beams.

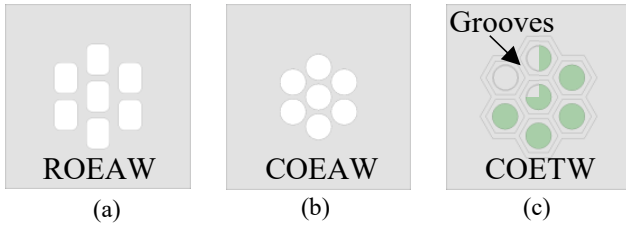

Figure 2.4: The FPA design considerations: (a) ROEAW-element-based FPA, (b) COEAW-element-based FPA, (c) COETW-element-based FPA with the grooves incorporated between the elements.

In relation to the aperture efficiency requirement, the beam-shaping techniques which allow for spillover and illumination efficiencies enhancement are discussed in the next Chapter. Moreover, element decoupling can improve the decoupling efficiency. The latter is also crucial when connecting FPA to the non-isolated beamformer, *e.g.* Rotman lens [58], or unified PC-BF network [44].

2.2 Design Considerations for Focal Plane Arrays

As a starting point, 7-element FPAs comprising open-ended waveguides arranged in the hexagonal lattice are considered. These designs include WG clusters of different element types, such as rectangular open-ended air-filled WG (ROEAW) [Fig. 2.4a], circular open-ended air-filled WG (COEAW)[Fig. 2.4b], and circular open-ended Teflon-filled WG (COETW) [Fig. 2.4c]. Table. 2.1 outlines the advantages and drawbacks of these designs.

Fig. 2.5 illustrates the performance of the considered FPA designs. The ROEAW and COEAW FPAs demonstrate mutual coupling level of around -23 dB between all elements and passive reflection coefficient level of ≈ -23 dB and ≈ -13 dB [Figs. 2.5(a),(b)]. Moreover, their EEPs have a large H-plane beamwidth at the relative amplitude taper of -10 dB. As seen, the COETW FPA performs slightly better, compared to the other designs, owing to the implemented grooves between the FPA elements result in mutual coupling reduction [$2-8$ dB, see Figs. 2.5(a)-(c)] and help to shape the *primary* EEP. The latter is especially important in the case of an offset reflector, since

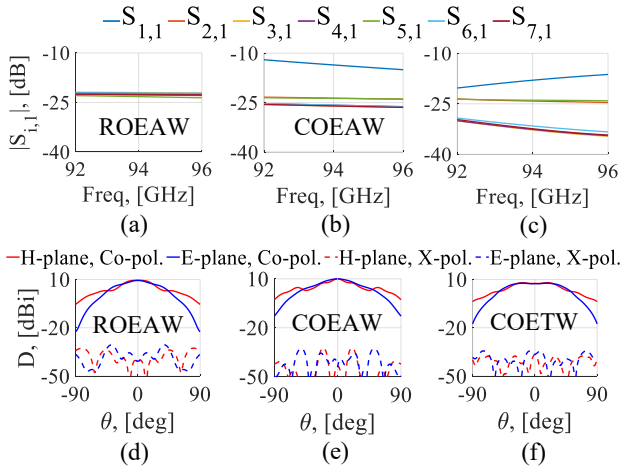

Figure 2.5: The performance of the considered FPA designs: (a)-(c) the S-parameters, and (d)-(f) the embedded far-field patterns of the central elements.

insufficient taper of the FPA EEP in the direction of reflector rim leads to high spillover and can deteriorate the aperture efficiency when the offset FPA element is excited.

In summary, the COETW FPA design shows promising performance, owing to the introduced features. However, the offset element EEP needs to be improved for use with the offset reflector antenna. At the same way, ROEAW is also aimed to be modified by introducing the decoupling features suitable for the case of small proximity between the elements and beam shaping of the offset element patterns. Chapter 3 will demonstrate the strategies for performance enhancement of the aforementioned FPA designs to facilitate higher aperture efficiency for the off-axis beams (offset elements *secondary* EEPs) and mitigate mutual coupling effects.

Table 2.1: Comparison of Element Types: Advantages and Design Complexities

Design Type	**Pros**	**Cons**
ROEAW	– Passive reflection coefficient ≤ -20 dB – Direct compatibility with rectangular waveguide interface – High radiation efficiency	– Relatively strong mutual coupling -22 dB, compared to COETW – Limited physical space between elements – Different radiation pattern cuts in E- and H-planes, degrading directivity
COEAW	– Relatively easy to manufacture at 100 GHz – High radiation efficiency – Extendable to dual-polarization without FPA aperture modification	– Relatively strong mutual coupling -23 dB, compared to COETW – Limited physical space between elements – Different far-field pattern in E- and H-planes, degrading directivity – Passive reflection coefficient ≤ -11 dB without matching circuitry
COETW	– Smaller element aperture vs. other types – More physical space between elements – More design degrees of freedom – Weaker mutual coupling (≤ -30 dB) – Extendable to dual-polarization without FPA aperture modification	– Higher loss due to Teflon – Difficult to manufacture

CHAPTER 3

Focal Plane Arrays Based on Open-Ended Waveguide: Design and Implementation

This chapter is focused on the implementation of waveguide-based FPAs, which are considered for the beam-switching/steering reflector antennas in the W-band. In particular, the decoupling and embedded-element pattern shaping techniques are utilized to design the element and FPA aperture layout. We illustrate that these techniques can enhance the aperture efficiency of the reflector antenna system, especially for the offset FPA elements, while improving scanning performance in combination with a non-isolated beamforming network.

3.1 FPA Element Design

In antenna arrays, mutual coupling effects can be a critical factor compromising impedance matching and scanning performance. This is particularly important for the considered FPA, which consists of a relatively small number of elements. In such cases, strong mutual coupling can significantly reduce the performance of the edge elements, including the far-field pattern shape and

reflection level.

Considering the array of WG openings, the apertures in the conductive plane are susceptible to the surface waves TM (to the normal). Therefore, a portion of the soft surface or high-impedance structure can be incorporated between the FPA elements to suppress surface wave propagation. Various techniques can be used to mitigate mutual coupling, such as grooves, AMC pins [64], decoupling networks [65], and etc. However, the use of these techniques is limited by the physical space available between the elements, which is typically determined by the inter-element spacing. Moreover, their implementation can influence the embedded-element pattern – especially critical for FPAs with a small number of elements – and must be carefully considered. This section focuses on exploring decoupling and embedded-pattern shaping strategies in the design of waveguide-based FPA elements.

COETW FPA with Inter-Element Grooves

As demonstrated in Chapter 2, the COETW-based FPA design, which includes the 0.25λ-depth inter-element grooves, reduces mutual coupling level and help to symmetrize FPA EEP. However, this design employs Teflon-filled WG element type with diameter of $D_{\mathrm{WG}} = 0.47\lambda$ at the central frequency $f_0 = 94$ GHz to ensure feasibility. This choice results in a relatively high passive reflection coefficient $|S_{ii}|$ of around -9 dB. Moreover, the implementation of inter-element grooves introduces additional reactance at the open-ended WG aperture, which influences $|S_{ii}|$. To address this, a matching WG section with a larger diameter is introduced in the WG aperture, which, in combination with the inter-element grooves, facilitates the $|S_{ii}| < -16$ dB. For comparison, the standalone matching WG section or inter-element grooves yield $|S_{ii}| < -11$ dB.

As mentioned above, nearly 0.25λ-depth grooves create a portion of the soft surface in the aperture of the FPA, thereby, affecting the shape of the far-field pattern. Here, the working principle resembles that of the choke ring horn. The axial symmetry of the structure ensures the azimuthal variation along the ring (groove) corresponding to $\sin(\varphi)$, which facilitates the symmetric far-field pattern. However, when the offset element is excited, the EEP becomes non-symmetric due to the more complicated mechanism of the groove contribution, particularly, multi-modal groove excitation.

Fig. 3.1 demonstrates the performance of the COETW FPA in the different

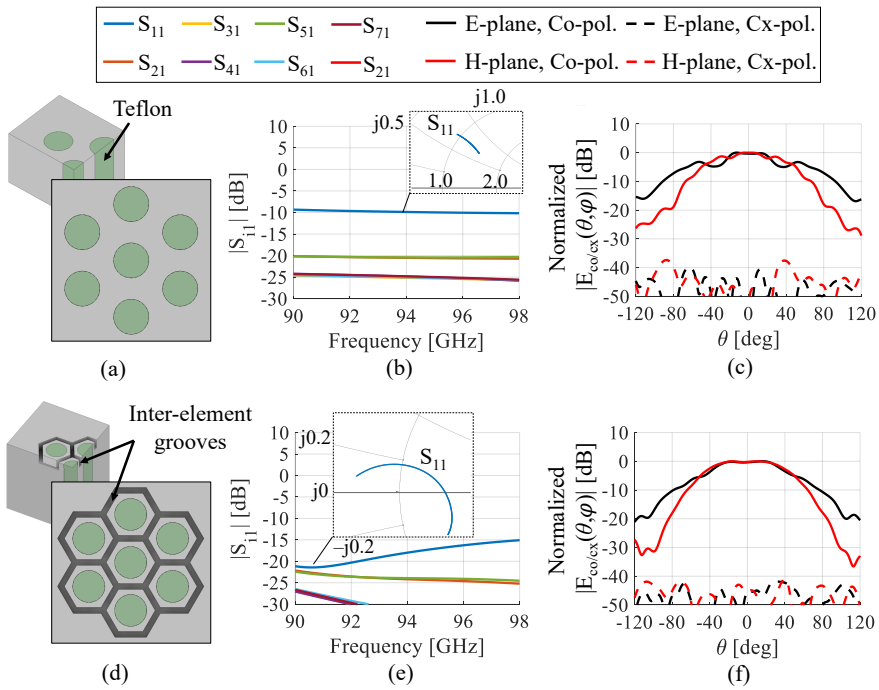

Figure 3.1: Performance of the FPA design comprising 7 COETW elements with and w/o inter-element grooves and matching section: (a), (d) the 3D geometry, (b), (e) the S-parameters, (c), (f) the EEP of the central element.

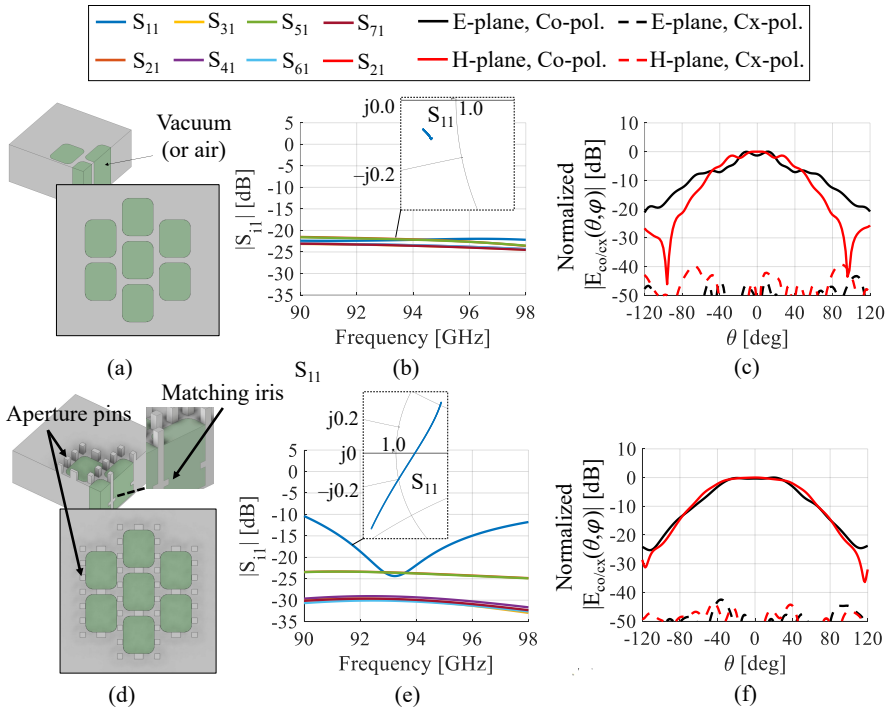

Figure 3.2: Performance of the FPA design comprising 7 ROEAW elements with and w/o aperture pins and matching iris: (a), (d) the 3D geometry, (b), (e) the S-parameters, (c), (f) the EEP of the central element.

design steps.

ROEAW FPA with Aperture Pins

On the basis of the results for the COETW FPA, the ROEAW FPA design [Fig. 3.2(a)] can be improved by incorporating a high-impedance structure in the aperture. Due to the limited space, the most suitable option was found to be a single row pin structure of nearly 0.25λ height in the aperture between the FPA elements (aperture pins). Fig. 3.2(d) shows the design of the ROETW FPA with aperture pins. Since the pins are introduced on the WG edges, they impact the passive reflection coefficient $|S_{ii}|$, making it inductive with the effect of transformation to the lower impedance. To compensate for this, the matching iris was introduced inside the WG at the distance from the aperture [Fig. 3.2(d)]. The latter introduces limitations in the achievable bandwidth for this design.

Fig. 3.2 demonstrates the performance of the ROEAW FPA in the different design steps. As shown, the aperture pins also affect the EEP, which is beneficial in terms of enhancing the aperture efficiency of the reflector antenna.

3.2 Array-Level Beam Shaping in FPA

The aperture pins/inter-element grooves cannot facilitate the required aperture efficiency for the reflector antenna system, when the offset element is excited: it varies from 64% for the central element to 43% for the offset element for ROEAW FPA with the aperture pins. Therefore, additional beam-shaping features need to be introduced to address this problem. Since there is no physical space between the FPA elements due to the introducing the decoupling/element-level beam shaping structures, the entire structure can be encircled by an exterior choke-ring pair formed by walls with distance $|R_{3,2} - R_{2,1}| < \lambda/2$. However, since element-level beam shaping structures act as a portion of the soft surface, choke rings cannot be excited effectively. The solution is to locate the choke rings in the staircase manner, which magnifies their contribution to the FPA EEPs.

The main drawback of incorporation of the exterior choke rings is the deterioration of the relative cross-polarization level from ≈ -22 dB up to -15 dB in the principal E- and H-planes, when the offset element is excited. To ex-

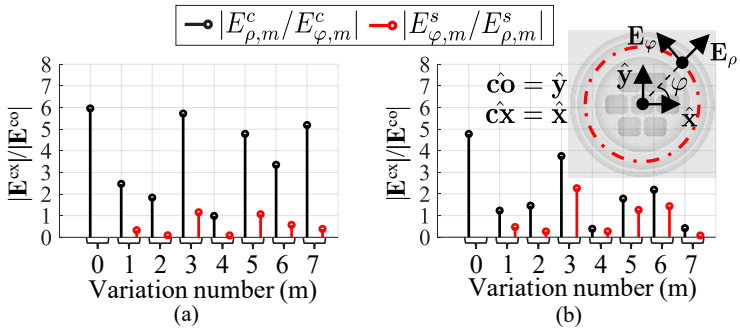

Figure 3.3: The choke ring azimuthal spectrum for the ROEAW FPA design with (a) the solid rings, (b) the perforated rings. Offset element #3 is excited.

plain this effect, the field of the first choke-ring, obtained numerically using full-wave simulation, can be analyzed along the central circumference. The field was decomposed into the set of azimuthal modes $E_m^{c/s}$, where the index m in the subscript corresponds to the order of variation with the $\cos(m\varphi)$ (index "c") or $\sin(m\varphi)$ (index "s") in the cylindrical coordinate system. Since the distance between the walls is $< \lambda/2$, the radial variation of the first order is dominant. Thus, each azimuthal mode $E_m^{c/s}$ includes the contribution of the various $\mathrm{TE}_{mn}^{c/s}$ and $\mathrm{TM}_{mn}^{c/s}$ modes of the corresponding coaxial WG with the same m-th azimuthal order. The FPA excitation strongly affects the modal distribution in the choke ring. As an example, the ROEAW FPA is considered. When, *e.g.*, the central element is excited, the structure preserves the axial symmetry, resulting only in the $m = 1$ order $\sin(m\varphi)$ variation or TE_{11}^{s}. However, when an offset element is excited, the path length difference between the points of the choke ring and the excited FPA element results in multi-modal ring excitation due to a non-uniform phase and amplitude profile. Thus, TEM and TE_{11}^{c} and other high-order modes are excited in addition to TE_{11}^{s}. The first two modes are the main contributors to the cross-polarization level in the H-plane.

For a quantitative evaluation of the contribution to the cross-polarization level from the azimuthal modes, the analysis is reduced to the principal E- and H-planes. In this case, the total cross-polarized modal field $\mathbf{E}_m^{cx}$ can be represented as $E_{\rho,m}^c$ and $E_{\varphi,m}^s$ with the corresponding co-polarized $\mathbf{E}_m^{co}$

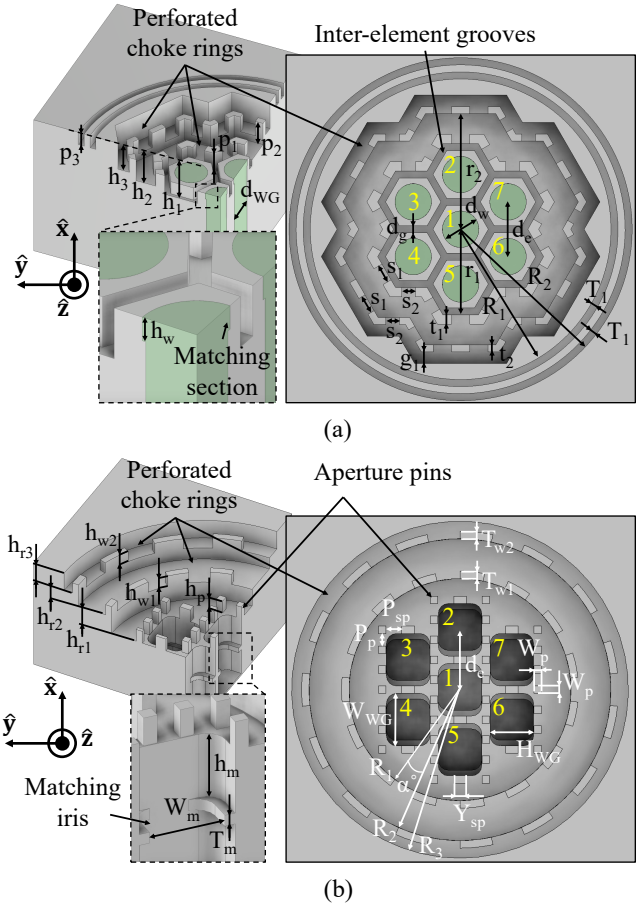

Figure 3.4: The final FPA designs: (a) the COETW FPA, (b) the ROEAW FPA. The introduced element enumeration is presented in yellow color and used further in the text.

represented as $E^{c}_{\varphi,m}$ and $E^{s}_{\rho,m}$. Fig. 3.3(a) demonstrates the relative cross-polarized modal components when an offset element of the ROEAW FPA with solid walls is excited.

Therefore, to mitigate the cross-polarization level related to the choke rings, periodic perforation of the sidewalls with a step of 12° was introduced. Fig. 3.3(b)

demonstrates the relative cross-polarized modal components when the offset element of the ROEAW FPA with perforated walls is excited. Notably, this modification reduces the $|E^c_{\rho,m}/E^c_{\varphi,m}|$ radio and suppresses the TEM and TE^c_{11}. The mode-filtering property of the sidewall perforation facilitates the reduction in relative cross-polarization down to ≤ -20 dB, while the co-polarized EEPs preserve their flat shape.

In summary, the use of the array-level beam shaping technique through the exterior choke-ring pair results in the increased FPA-fed reflector antenna aperture efficiency up to $52-68\%$ from $43-64\%$ for the baseline design without choke-rings. Fig. 3.4 illustrates the final COETW and ROEAW FPA designs. The geometric parameters of both designs are summarized in Table 3.1.

Table 3.1: Geometric parameters of the final FPA designs. Dimensions are given in mm.

COETW FPA design					
Parameter	Value	Parameter	Value	Parameter	Value
d_w	1.6	h_1	2.35	p_1	1.15
d_e	2.4	h_2	2	p_2	1.3
d_g	0.3	h_3	1.6	p_3	0.75
r_1	3.75	t_1	0.4	g_1	0.5
r_2	5.05	t_2	0.3	T_1	0.3
s_1	0.8	s_2	0.6	R_1	6.6
R_2	7.21	h_w	0.35	d_WG	1.5
ROEAW FPA design					
Parameter	Value	Parameter	Value	Parameter	Value
H_WG	1.74	d_e	2.4	h_r1	0.9
h_r2	0.6	h_r3	0.95	h_w1	0.55
h_w2	0.5	h_p=P_sp	0.64	h_m	1.52
T_m	0.25	P_p=Y_sp	0.5	W_WG	2.1
W_m	1.6	α	12°	T_w1=T_w2=W_p	0.3
R_1	4.45	R_2	6.05	R_3	6.75

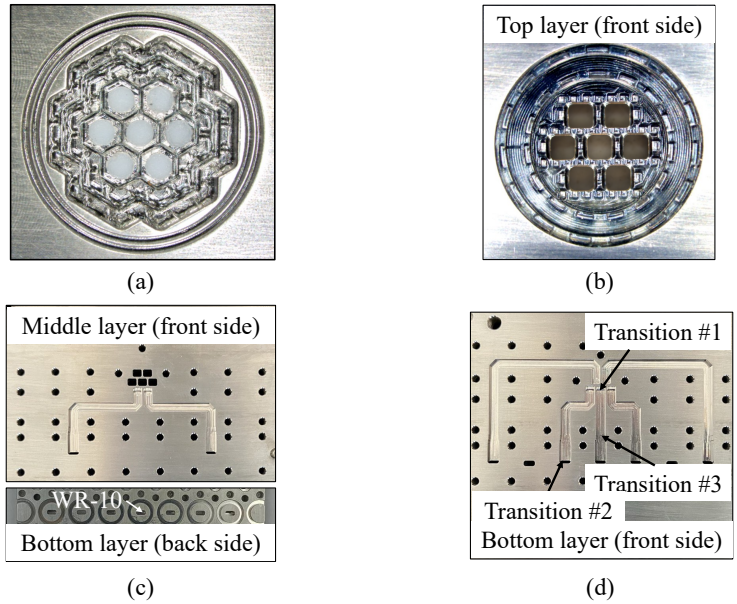

Figure 3.5: The final FPA prototypes: (a) the COETW FPA, (b) the ROEAW FPA, (c) the middle layer of the ROEAW FPA, and (d) the bottom layer of the ROEAW FPA.

3.3 FPA Prototyping and Measurements

The prototypes of the FPA designs were fabricated to experimentally verify the performance of the designed arrays. In particular, the FPA apertures were manufactured using Electrical-Discharge Molding (EDM) for COETW FPA, and CNC machining for the ROEAW FPA. Each FPA prototype comprises three metal layers, with the FPA aperture on the top layer and WG feeding network on the other layers. The FPA apertures are shown in Fig. 3.5(a),(b). Fig. 3.5(c),(d) demonstrates the ROEAW FPA feeding network including WG fan-out, where each WG channel has two inter-layer orthogonal transitions [#1, #2 in Fig. 3.5(d)], and an H-plane transition between the customized feeding WG (2.1×1.27 mm^2 cross-section) and the standard WR-10 WG interface (transition #3) used in the measurement setup.

Fig. 3.6 demonstrates that the simulated and measured S-parameters of the

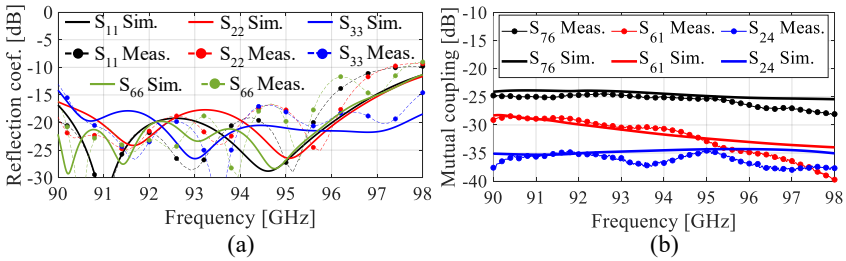

Figure 3.6: The simulated and measured S-parameters of the ROEAW: (a) passive reflection coefficients $|S_{ii}|$, (b) mutual coupling coefficients $|S_{ji}|$.

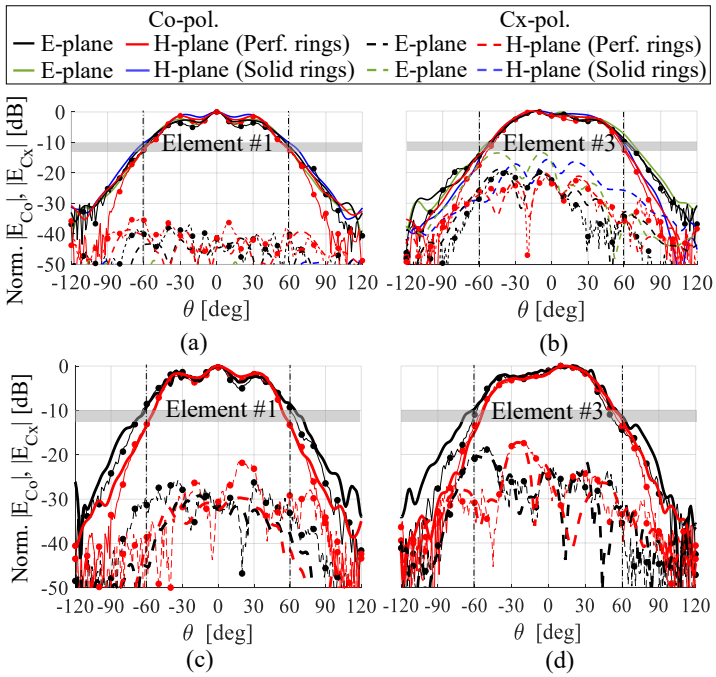

Figure 3.7: The simulated (solid) and measured (symbol) FPA EEPs: (a) ROEAW central element #1, (b) ROEAW offset element #3, (c) COETW central element #1, and (d) COETW offset element #3.

ROEAW FPA are in good agreement. In the targeted bandwidth, $|S_{ij}| < -25$ dB, and $|S_{ii}| < -17$ dB for all elements except for a small region around 96 GHz for elements #6 and #7, where these values reach -13 dB. Fig. 3.7 demonstrates the EEPs which were measured for both FPA prototypes.

3.4 FPA-fed Reflector Antenna Performance

The performance of the reflector antenna presented in the Fig. 2.3 was evaluated using GRASP software utilizing a combined Physical Optics and Physical Theory of Diffraction method. The measured FPA patterns include 24 cuts within $0° \leq \theta \leq 180°$, and $0° \leq \varphi \leq 360°$ with a step in azimuth $\Delta\varphi = 15°$. Fig. 3.8 illustrates the 2D colormap of the reflector antenna EEPs (*secondary* EEPs) and patterns cuts with the peak gain and cross-over level. As seen, the designed reflector antenna system is capable of beam-steering within 1° 2D angular range with < 5 dB gain loss. This meets the system design goals.

3.5 Beam-Steering and Scalability

The proposed FPA can be used as a phased array feed to realize continuous beam-steering, when all FPA elements are utilized in the beamforming. This is equivalent to the beam-steering antenna front-end architecture #1 (Sec. 1.5). In this analysis, the maximum gain beamforming approach (conjugate field matching, CFM) is chosen, which is common for point-to-point communication applications. The reflector antenna *secondary* EEPs were used to generate multiple steered beams within the 1.5° 2D angular range with the steps $\Delta\theta = 0.1°$ and $\Delta\varphi = 5°$. Fig. 3.9(a) shows the 2D gain profile for the beam-steering reflector antenna with the phased FPA. According to the sampling theorem, the gain of the generated steered beams have oscillating variations (ripples), if the FPA inter-element spacing is $> 0.5\lambda$. As anticipated, the ripples of 1 dB can be observed in Fig. 3.9(a) as perturbations in the gain profile. According to the criterion of maximum 6 dB beam scan loss, the scanning range of the proposed reflector antenna system is limited by the 1° 2D range, which is constrained by the size of the FPA aperture.

To demonstrate the scanning performance of the utilized reflector antenna system and the scalability of the proposed FPA design, the ROEAW FPA was extended to a 19-element FPA by adding one more "ring" of elements utilizing

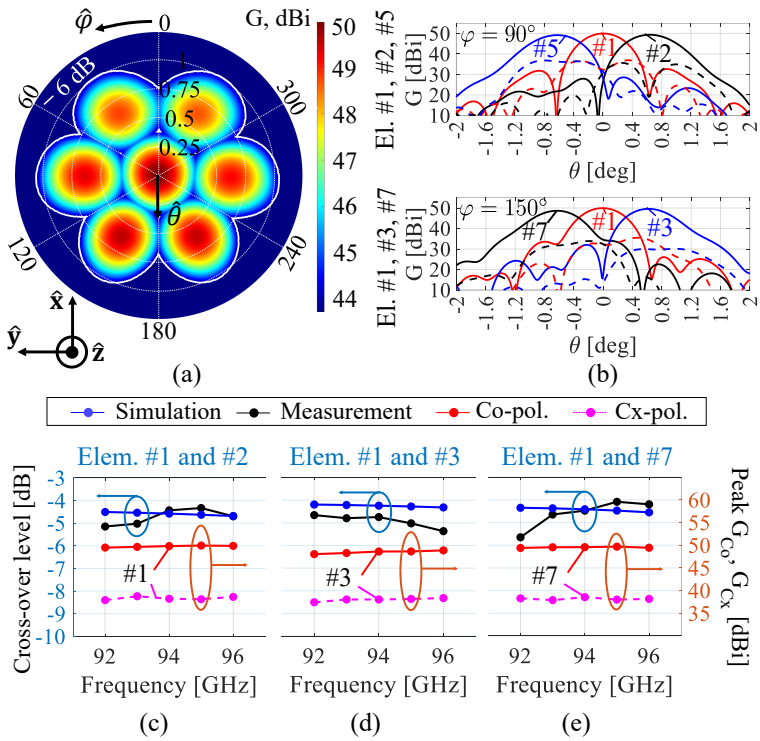

Figure 3.8: The *secondary* EEPs calculated in GRASP using the measured FPA EEPs of the ROEAW: (a) colormap of overlapping beams corresponding to the *secondary* EEPs (or one-element-per-beam configuration), (b) *secondary* EEP cuts, (c)-(e) the peak gain and beam cross-over level.

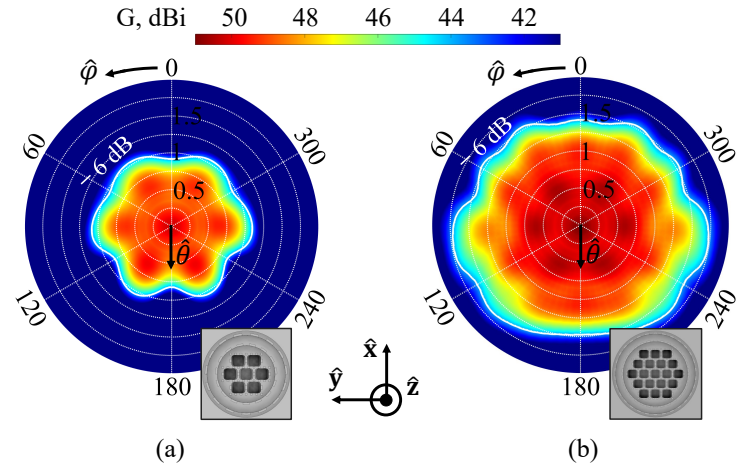

Figure 3.9: The simulated beamformed *secondary* far-field pattern gain profile for the ROEAW FPA: (a) 7-element FPA, (b) 19-element FPA.

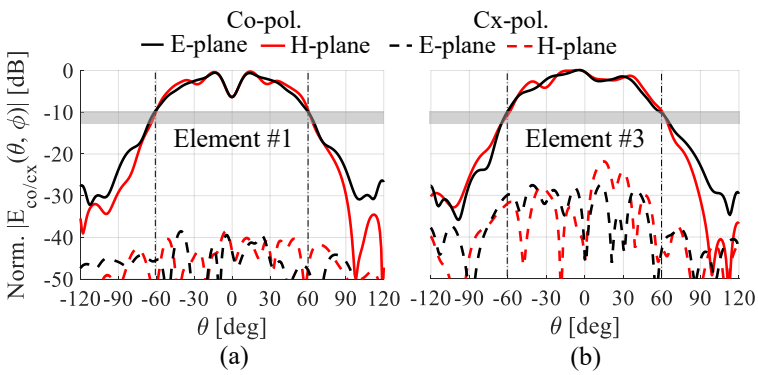

Figure 3.10: The simulated the 19-element ROEAW FPA *primary* EEPs: (a) central element #1, (b) offset element #3. The element enumeration corresponds to the one used for the 7-element FPA.

the same decoupling and beam-shaping techniques. To mitigate the increase in cross-polarization level caused by introducing the choke-ring pair, the choke ring wall perforation period was reduced from 12° to 6°. The *primary* FPA EEPs [Fig. 3.10] were used to compute *secondary* EEPs and beamformed far-

field patterns. The resultant 2D gain profile is presented in Fig. 3.9(b). As shown, the angular scanning range is enhanced up to 1.5° (2.5HPBW) in 2D, which approaches the theoretical limit for this reflector [60]. The gain profile ripple is reduced down to 0.4 dB withing the 1° 2D angular range, which can be explained by more degrees of freedom (number of elements with individual complex-valued excitation coefficients) in optimizing the illumination of the reflector aperture.

In summary, the proposed FPA design can be utilized as a part of the beam-steering reflector antenna system, offering the desired illumination of the reflector for high aperture efficiency. The enhanced scanning range can be achieved as a result of a straightforward scaling procedure, *i.e.* adding more "rings" of the array elements without significant design modifications.

CHAPTER 4

Summary of included papers

This chapter provides a summary of the included papers.

4.1 Paper A

Viktor Chernikov, Artem Vilenskiy, Marianna Ivashina
Analysis of Millimeter-Wave Array Frontend Architectures for High EIRP: Comparing Various Beamforming and Power Combining Techniques
19th European Conference on Antennas and Propagation, EuCAP 2025, Stockholm, Sweden, Apr. 2025.
 DOI 10.23919/EuCAP63536.2025.10999899 .

This paper analyzes various beamforming array antenna front-end architectures for high-data-rate point-to-point communication over long distances. The analysis focuses on W-band wireless backhaul applications, addressing key challenges, such as efficient mmWave RF power generation and accurate beam-steering through advanced antenna design. Based on state-of-the-art research, different beamforming array designs are compared. To support the analysis, simplified models of array transmitters are used, incorporating litera-

ture data and based on our design experience with commercial (PIN-)pHEMT (Al)GaAs processes. To illustrate these concepts, a case study of a 50 dBi reflector antenna fed by a focal plane array (phased array feed) designed for W-band backhaul links is presented. The design curves obtained from this analysis show the trade-offs to achieve high performance with minimal energy consumption.

4.2 Paper B

Viktor Chernikov, Artem Vilenskiy, Marianna Ivashina
Design Considerations for Focal-Plane Array Antennas for 6G Millimeter-Wave Backhaul Links
2023 IEEE International Symposium on Antennas and Propagation and USNC-URSI Radio Science Meeting, AP-S/URSI 2023,
Portland, USA, July 2023.
 DOI 10.1109/USNC-URSI52151.2023.10237794 .

This work presents three designs of W-band Focal-Plane Array (FPA) antennas as possible candidates for the next-generation millimeter-wave (mmWave) backhaul links. The considered FPAs comprise different types of waveguide antenna elements and are used to feed a prime-focus reflector with 400 mm aperture diameter. The main design goal is to achieve high directivity (50 dBi) with minimal beam scan loss, while complying with the strict side-lobe level requirements (ETSI class 3).

4.3 Paper C

Viktor Chernikov, Artem Vilenskiy, Sam Agneessens, Lars Manholm, Malcolm Ng Mou Kehn, Marianna Ivashina
A Teflon-Filled Open-Ended Circular Waveguide Focal-Plane-Array Used for Sway Compensation in W-band 50dB-Gain Backhaul Reflector Antennas
25th International Conference on Electromagnetics in Advanced Applications, ICEAA 2023,

Venice, Italy, Oct. 2023.
 DOI 10.1109/ICEAA57318.2023.10297687 .

The paper introduces a focal plane array (FPA) design aimed at enhancing the reliability of millimeter-wave backhaul communication links by compensation of the mast swaying. This FPA is designed for an offset parabolic reflector antenna with the 400 mm aperture diameter at W-band frequencies (92–96 GHz). The analysis of the total reflector-FPA system shows promising results, i.e. $56-68\%$ antenna aperture efficiency ($49-50$ dBi directivity) for all beams with compliance to the radiation emission constraints (ETSI class 3) within $\pm 89^\circ$ and high cross-over level > -6 dB.

4.4 Paper D

Viktor Chernikov, Artem Vilenskiy, Sam Agneessens, Lars Manholm, Marianna Ivashina
A W-Band Choke-Ring Encircled Focal Plane Array of Full-Metal Elements for Reflector Antennas with over 50%-Efficiency High Cross-Over Beams
IEEE Antennas and Wireless Propagation Letters,
Vol. 23 Issue 12 pp. 4578-4582, Dec. 2024.
 DOI 10.1109/LAWP.2024.3458182 .

This work presents a W-band (92–96 GHz) focal plane array (FPA) for 50 dBi-reflector antennas. The FPA comprises seven metal waveguide elements arranged in a hexagonal lattice with decoupling single-row pin structure (aperture pins) facilitating < -24 dB mutual coupling level. The FPA performance, evaluated on an offset parabolic reflector with F/D=0.35, exhibits 52-68% efficiency, close beam overlap with cross-over level > -6 dB, and passive reflection coefficient of < -15 dB. Measurements of the FPA prototype verify the results for all characteristics; the latter are competitive with state-of-the-art solutions.

CHAPTER 5

Concluding Remarks and Future Work

This research introduces two W-band focal plane array (FPA) designs based on rectangular air-filled and circular Teflon-filled waveguide radiating elements, thereby contributing to the advancement of 5G/6G wireless communication systems at mmWave frequencies. Specifically, these FPAs are employed as feeds for reflector antennas, enabling electronic beam-steering, which is a promising approach for compensating mast sway in W-band point-to-point long-distance applications. The proposed FPAs are designed for $92 - 96$ GHz (W-band) operation, addressing challenges such as high radiation efficiency, small element proximity, and efficient reflector illumination. Therefore, these design improvements offer advantages over existing solutions by supporting high antenna gain and the potential for rapid electronic beam-steering capabilities.

To enhance the performance of the baseline designs, *i.e.* 7-element cluster comprising circular open-ended Teflon-filled waveguide or rectangular open-ended air-filled waveguide radiating elements, specialized decoupling and beam-shaping techniques were implemented both at the element- and array-levels to maximize aperture efficiency. To mitigate mutual coupling effects between elements, two dedicated decoupling techniques, such as inter-element grooves,

and aperture pins, were implemented. This results in a reduction of the mutual coupling level varying within the $2-7$ dB range, compared to the baseline design, depending on the antenna element position. Furthermore, the introduced features contribute to element-level beam shaping leading to more uniform illumination of the reflector maintaining the required amplitude taper. Particularly, this allows to enhance the reflector antenna aperture efficiency by 8% (0.35 dB). It is worth mentioning that these techniques can be employed in more general cases of 2D antenna arrays. The introduced choke-ring pair results in the array-level beam shaping and reflector antenna aperture efficiency enhancement by additional 10% (0.42 dB) for the offset elements. This technique can be utilized to further fine-tune far-field patterns of open-ended waveguide or horn antenna clusters.

The waveguide-based implementation of the proposed FPAs facilitates integration with waveguide beamforming networks, as commonly used in the W-band. This compatibility supports the development of the active antenna system that enables efficient power combining and beamforming in an active transmitter front-end.

In conclusion, the proposed focal plane array designs fill the gap in current mmWave antenna technologies and represent an important step in the development of waveguide-based active reflector antenna systems in the W-band. These solutions provide a platform for high-performance, electronically steerable antennas suited for the next-generation wireless communication systems.

Future research will focus on the full integration and implementation of the active transmitter front-end with the proposed reflector antenna system, aligned with the front-end architecture #3 in Fig. 1.8c. The work will involve the characterization of the entire system, including the passive antenna system part with the beamforming network, and the active system performance in terms of the achievable Equivalent Isotropic Radiated Power ($EIRP$), transmitter output power, and scanning range. The final goal of the PhD thesis is the demonstration of a fully functional, integrated W-band active antenna system. This includes the use of a 6-channel active module developed in Gotmic AB and specifications provided by Ericsson Research within the ENERGETIC project.

References

[1] "5g explained." (), [Online]. Available: https://www.ericsson.com/en/5g.

[2] "Backhaul capacity evolution." (2024), [Online]. Available: https://www.ericsson.com/en/reports-and-papers/microwave-outlook/articles/backhaul-capacity-evolution.

[3] "Deutsche telekom, cosmote and ericsson look beyond 100GHz to boost 5G backhaul capacity." (2021), [Online]. Available: https://www.ericsson.com/en/news/2021/4/ericsson-trials-w-band-as-5g-%20backhaul-spectrum.

[4] "Hua Wang, Mohamed Eleraky, Basem Abdelaziz, Bryan Lin, Edward Liu, Yuqi Liu, Mohsen Ghorbanpoor, Chenhao Chu, Andrea Ruffino, Jinglong Xu, Filippo Svelto, Niccolò Villaggi, Abdelrahman Habib, Kyungsik Choi, Tzu-Yuan Huang, Hossein Jalili, Naga Sasikanth Mannem, Jeongsoo Park, Jeongseok Lee, David Munzer, Sensen Li, Fei Wang, Amr S. Ahmed, Christopher Snyder, Huy Thong Nguyen, and Michael Edward Duffy Smith: Power amplifiers performance survey 2000-present." (2023), [Online]. Available: https://ideas.ethz.ch/research/surveys/pa-survey.html.

[5] P. Song, A. C. Ulusoy, R. L. Schmid, S. N. Zeinolabedinzadeh, and J. D. Cressler, "W-band sige power amplifiers," in *2014 IEEE Bipolar/BiCMOS Circuits and Technology Meeting (BCTM)*, 2014, pp. 151–154.

[6] C. R. Chappidi and K. Sengupta, "A W-band SiGe power amplifier with psat of 23 dbm and pae of 16.8% at 95ghz," in *2017 IEEE MTT-S International Microwave Symposium (IMS)*, 2017, pp. 1699–1702.

[7] M. Micovic, A. Kurdoghlian, A. Margomenos, *et al.*, "92–96 ghz gan power amplifiers," in *2012 IEEE/MTT-S International Microwave Symposium Digest*, 2012, pp. 1–3.

[8] P. Huang, E. Lin, R. Lai, *et al.*, "A 94 ghz monolithic high output power amplifier," in *1997 IEEE MTT-S International Microwave Symposium Digest*, vol. 3, 1997, 1175–1178 vol.3.

[9] J. Du, E. Onaran, D. Chizhik, S. Venkatesan, and R. A. Valenzuela, "Gbps user rates using mmwave relayed backhaul with high-gain antennas," *IEEE Journal on Selected Areas in Communications*, vol. 35, no. 6, pp. 1363–1372, 2017.

[10] M. Marcus and B. Pattan, "Millimeter wave propagation: Spectrum management implications," *IEEE Microwave Magazine*, vol. 6, no. 2, pp. 54–62, 2005.

[11] *Fixed Radio Systems; Characteristics and requirements for point-to-point equipment and antennas; Part 4-2: Antennas; Harmonized EN covering the essential requirements of article 3.2 of the R&TTE Directive*, Harmonized European Standard (Telecommunications series), ETSI, Jan. 2010.

[12] "Sway compensation antennas, your E-band friend, with benefits." (2023), [Online]. Available: `https://www.ericsson.com/en/blog/2023/3/sway-compensation-antennas`.

[13] "Ericsson micrwave outlook 2021." (2021), [Online]. Available: `https://www.ericsson.com/en/reports-and-papers/microwave-outlook/reports/2021`.

[14] S. Shahramian, M. J. Holyoak, A. Singh, and Y. Baeyens, "A fully integrated 384-element, 16-tile, *W*-band phased array with self-alignment and self-test," *IEEE Journal of Solid-State Circuits*, vol. 54, no. 9, pp. 2419–2434, 2019.

[15] J. Ala-Laurinaho, J. Aurinsalo, A. Karttunen, *et al.*, "2-D beam-steerable integrated lens antenna system for 5G E-band access and backhaul," *IEEE Transactions on Microwave Theory and Techniques*, vol. 64, no. 7, pp. 2244–2255, 2016.

[16] E. Wang, S. Agneessens, O. Talcoth, *et al.*, "A 50 dBi E-Band dual-reflector antenna for 5G backhauling with auto-beam-tracking function," *IEEE Transactions on Antennas and Propagation*, vol. 72, no. 6, pp. 4874–4887, 2024.

[17] B. Rohrdantz, T. Jaschke, T. Reuschel, S. Radzijewski, A. Sieganschin, and A. F. Jacob, "An electronically scannable reflector antenna using a planar active array feed at Ka-band," *IEEE Transactions on Microwave Theory and Techniques*, vol. 65, no. 5, pp. 1650–1661, 2017.

[18] A. Elsakka, A. Farsaei, A. J. van den Biggelaar, *et al.*, "A mm-wave phased-array fed torus reflector antenna with ±30° scan range for Massive-MIMO base-station applications," *IEEE Transactions on Antennas and Propagation*, vol. 70, no. 5, pp. 3398–3410, 2022.

[19] J.-L. A. Lijarcio, A. Vosoogh, V. Vassilev, *et al.*, "Substrate-less vertical chip-to-waveguide transition for w-band array antenna integration," in *2023 17th European Conference on Antennas and Propagation (EuCAP)*, 2023, pp. 1–3.

[20] A. R. Vilenskiy and Y. Zhang, "A compact and wideband mmic-to-ridge gap waveguide contactless transition for phased array antenna front ends," *IEEE Antennas and Wireless Propagation Letters*, vol. 23, no. 3, pp. 990–994, 2024.

[21] A. U. Zaman, V. Vassilev, P.-S. Kildal, and H. Zirath, "Millimeter wave e-plane transition from waveguide to microstrip line with large substrate size related to mmic integration," *IEEE Microwave and Wireless Components Letters*, vol. 26, no. 7, pp. 481–483, 2016.

[22] S. Shahramian, M. J. Holyoak, and Y. Baeyens, "A 16-element W-band phased-array transceiver chipset with flip-chip PCB integrated antennas for multi-gigabit wireless data links," *IEEE Transactions on Microwave Theory and Techniques*, vol. 66, no. 7, pp. 3389–3402, 2018.

[23] A. Natarajan, A. Valdes-Garcia, B. Sadhu, S. K. Reynolds, and B. D. Parker, "W-band dual-polarization phased-array transceiver front-end in sige bicmos," *IEEE Transactions on Microwave Theory and Techniques*, vol. 63, no. 6, pp. 1989–2002, 2015.

[24] D. Zhao, P. Yu, S. Jiang, W. Gao, P. He, and H. Liu, "W-band CMOS beamforming ICs and integrated phased-array antennas with 20+ gb/s data rates," *Science China Information Sciences*, vol. 67, no. 11, p. 212 301, 2024.

[25] W. Shin, B.-H. Ku, O. Inac, Y.-C. Ou, and G. M. Rebeiz, "A 108–114 GHz 4 $\times$ 4 wafer-scale phased array transmitter with high-efficiency on-chip antennas," *IEEE Journal of Solid-State Circuits*, vol. 48, no. 9, pp. 2041–2055, 2013.

[26] A. Dubok, A. Al-Rawi, N. Tessema, *et al.*, "Double-reflector configuration for optimal exposure of wideband focal-plane arrays with optical beamforming," *IEEE Transactions on Antennas and Propagation*, vol. 65, no. 8, pp. 4316–4321, 2017.

[27] H. Chreim, R. Chantalat, M. Thèvenot, *et al.*, "An enhanced Ka-band reflector focal-plane array using a multifeed EBG structure," *IEEE Antennas and Wireless Propagation Letters*, vol. 9, pp. 1152–1156, 2010.

[28] A.-E. Mahmoud, W. Hong, Y. Zhang, and A. Kishk, "W-band mutlilayer perforated dielectric substrate lens," *IEEE Antennas and Wireless Propagation Letters*, vol. 13, pp. 734–737, 2014.

[29] Z. Cao, Z. Liu, H. Meng, and W. Dou, "Design of w-band microstrip antenna array," in *2019 IEEE Asia-Pacific Microwave Conference (APMC)*, 2019, pp. 1319–1321.

[30] A. Al-Rawi, A. Dubok, S. J. Geluk, B. P. de Hon, M. H. A. J. Herben, and A. B. Smolders, "Increasing the eirp by using fpa-fed reflector antennas," in *2016 IEEE International Symposium on Antennas and Propagation (APSURSI)*, 2016, pp. 1623–1624.

[31] M. Ivashina and C. v. Klooster, "Focal fields in reflector antennas and associated array feed synthesis for high efficiency multi-beam performances," *TIJDSCHRIFT-NERG*, vol. 68, no. 1, pp. 11–19, 2003.

[32] E. Wang, "Millimeter-wave high-gain antenna for 5G backhauling with auto-beam-tracking function," Licentiate thesis, Department of Electrical Engineering, Chalmers University of Technology, Gothenburg, Sweden, Dec. 2023.

[33] E. G. Geterud, J. Yang, T. Ostling, and P. Bergmark, "Design and optimization of a compact wideband hat-fed reflector antenna for satellite communications," *IEEE Transactions on Antennas and Propagation*, vol. 61, no. 1, pp. 125–133, 2012.

[34] K. F. Warnick, R. Maaskant, M. V. Ivashina, D. B. Davidson, and B. D. Jeffs, *Phased arrays for radio astronomy, remote sensing, and satellite communications*. Cambridge University Press, 2018.

[35] M. V. Ivashina, M. N. M. Kehn, P.-S. Kildal, and R. Maaskant, "Decoupling efficiency of a wideband vivaldi focal plane array feeding a reflector antenna," *IEEE Transactions on Antennas and Propagation*, vol. 57, no. 2, pp. 373–382, 2009.

[36] P. Deo, M. Robinson, B. Maffei, G. Pisano, and N. Trappe, "W-band planar antennas for next generation sub-millimeter focal plane arrays," in *Millimeter, Submillimeter, and Far-Infrared Detectors and Instrumentation for Astronomy VIII*, SPIE, vol. 9914, 2016, pp. 949–957.

[37] Z. Chen, C.-C. Wang, H.-C. Yao, and P. Heydari, "A bicmos w-band 2× 2 focal-plane array with on-chip antenna," *IEEE Journal of Solid-State Circuits*, vol. 47, no. 10, pp. 2355–2371, 2012.

[38] Y. Wang, Y. Chen, and H. Meng, "Design of a W-band multi-beam antenna fed by sixteen feed-horns array," in *2020 IEEE MTT-S International Wireless Symposium (IWS)*, IEEE, 2020, pp. 1–3.

[39] K. Devaraj, S. Church, K. Cleary, *et al.*, "Argus: A w-band 16-pixel focal plane array for the green bank telescope," in *2014 United States National Committee of URSI National Radio Science Meeting (USNC-URSI NRSM)*, IEEE, 2014, pp. 1–1.

[40] E. Wang, T. Zhang, A. U. Zaman, *et al.*, "A compact gap-waveguide dual-polarized Ka-band feed for 50dBi reflector antennas with tracking function," *IEEE Access*, vol. 10, pp. 91 622–91 630, 2022.

[41] J. Johansson and P. Ingvarson, "Array antenna activities at ruag space: An overview," in *2013 7th European Conference on Antennas and Propagation (EuCAP)*, IEEE, 2013, pp. 666–669.

[42] M. N. M. Kehn and P.-S. Kildal, "Miniaturized rectangular hard waveguides for use in multifrequency phased arrays," *IEEE Transactions on Antennas and Propagation*, vol. 53, no. 1, pp. 100–109, 2005.

[43] M. N. M. Kehn, M. Ivashina, and L. Shafai, "Performance of multi-beam reflectors fed by phased array feeds with impedance-matching layers," in *2010 IEEE Antennas and Propagation Society International Symposium*, 2010, pp. 1–4.

[44] A. R. Vilenskiy, S. Y. Chaudhry, H.-T. Chou, and M. V. Ivashina, "Millimeter-wave array antenna architectures employing joint power combining and beam steering for next-generation backhaul applications," in *2023 17th European Conference on Antennas and Propagation (EuCAP)*, IEEE, 2023, pp. 1–5.

[45] K. Ma, S. Mou, Y. Lu, L. K. Meng, and K. S. Yeo, "A 60ghz defected ground power divider using sige bicmos technology," in *2011 International SoC Design Conference*, 2011, pp. 1–4.

[46] A. Wentzel, V. Subramanian, A. Sayed, and G. Boeck, "Novel broadband wilkinson power combiner," in *2006 European Microwave Conference*, 2006, pp. 212–215.

[47] J. Li, L. Li, L. Lu, H. Shi, H. Huo, and A. Zhang, "Four-way waveguide power divider design for w-band applications," *International Journal of RF and Microwave Computer-Aided Engineering*, vol. 28, no. 5, e21242, 2018.

[48] H. J. du Toit and D. I. L. de Villiers, "A fully isolated n-way radial power combiner," *IEEE Transactions on Microwave Theory and Techniques*, vol. 68, no. 7, pp. 2531–2538, 2020.

[49] H. Cheng, X. Zhu, F. Hou, W. Wang, L. Shen, and S. Hu, "Compact 31-w 96-ghz amplifier module in gan-mems for wireless communications," *IEEE Transactions on Microwave Theory and Techniques*, vol. 70, no. 2, pp. 1233–1241, 2022.

[50] H. Cheng, X. Zhu, J. Du, and W. Wang, "A terahertz gan solid-state power amplifier on radial combining technique," *Microwave and Optical Technology Letters*, vol. 66, no. 4, e34164, 2024.

[51] K. Eccleston, Q.-C. Sun, and S. Yeo, "Tapered microstrip line power combiners with colinear input ports," *Microwave and optical technology letters*, vol. 15, no. 6, pp. 339–342, 1997.

[52] A. Roev, "Wideband watt-level spatial power-combined power amplifier in sige bicmos technology for efficient mm-wave array transmitters," English, Proefschrift., Phd Thesis 1 (Research TU/e / Graduation TU/e), Electrical Engineering, Chalmers University of Technology, Aug. 2021.

[53] R. Maaskant, W. A. Shah, A. U. Zaman, M. Ivashina, and P.-S. Kildal, "Spatial power combining and splitting in gap waveguide technology," *IEEE Microwave and Wireless Components Letters*, vol. 26, no. 7, pp. 472–474, 2016.

[54] C. Yi, H. Lee, K. J. Lee, J. H. Joo, J. B. Kwon, and M. Kim, "Uniform-field over-mode waveguide for spatial power-combining applications," *IEEE Microwave and Wireless Components Letters*, vol. 28, no. 1, pp. 10–12, 2018.

[55] M. DeLisio and R. York, "Quasi-optical and spatial power combining," *IEEE Transactions on Microwave Theory and Techniques*, vol. 50, no. 3, pp. 929–936, 2002.

[56] D. Wang, K.-D. Xu, Y. Cao, C. Guo, and S. Yan, "A butler matrix-based multibeam w-band slot antenna array fabricated by metal additive manufacturing technology," *IEEE Transactions on Antennas and Propagation*, vol. 72, no. 6, pp. 5349–5354, 2024.

[57] J. S. Park, T. Chi, and H. Wang, "An ultra-broadband compact mm-wave butler matrix in cmos for array-based mimo systems," in *Proceedings of the IEEE 2013 Custom Integrated Circuits Conference*, 2013, pp. 1–4.

[58] D. Nüßler and H.-H. Fuchs, "A rotman lens at w-band," *Frequenz*, vol. 56, no. 11-12, pp. 244–248, 2002.

[59] *gAPZ0095A W-band power amplifier 92-96 GHz (85-100 GHz)*, Accessed on October 14, 2024, 2024.

[60] T. A. Milligan, *Modern antenna design*. John Wiley & Sons, 2005.

[61] P.-S. Kildal, *Foundations of antenna engineering: a unified approach for line-of-sight and multipath*. Artech House, 2015.

[62] T. Teshirogi and T. Yoneyama, *Modern millimeter-wave technologies*. Ios Press, 2001.

[63] S. López-Ruiz, R. Sanchez Montero, F. Tercero-Martínez, P. López-Espí, and J. López-Fernandez, "Optimization of a conical corrugated antenna using multiobjective heuristics for radio-astronomy applications," *International Journal of Antennas and Propagation*, vol. 2016, no. 1, p. 7 024 704, 2016.

[64] Y. Zhang, A. R. Vilenskiy, and M. V. Ivashina, "Mutual coupling analysis of open-ended ridge and ridge gap waveguide radiating elements in an infinite array environment," in *2022 52nd European Microwave Conference (EuMC)*, IEEE, 2022, pp. 696–699.

[65] A. A. Diman, F. Karami, P. Rezaei, *et al.*, "Efficient siw-feed network suppressing mutual coupling of slot antenna array," *IEEE Transactions on Antennas and Propagation*, vol. 69, no. 9, pp. 6058–6063, 2021.